

Aus dem Lehrstuhl Anatomie II – Neuroanatomie der Anatomischen Anstalt
der Ludwig-Maximilians-Universität München

Vorstand: Univ. Prof. Dr. med. Christoph Schmitz

***Neurodegeneration in
multiple sclerosis mouse models***

Dissertation
zum Erwerb des Doktorgrades der Medizin
an der Medizinischen Fakultät der
Ludwig-Maximilians-Universität zu München

vorgelegt von

Sebastian Rühling

aus

Böblingen

2021

Mit Genehmigung der Medizinischen Fakultät
der Universität München

Berichterstatter: Prof. Dr. med. Dr. rer. nat. Markus Kipp

Mitberichterstatter: Prof. Dr. Dieter Edbauer
PD Dr. Klaus Dornmair
Prof. Dr. Harald Steiner

Mitbetreuung durch den
promovierten Mitarbeiter: Dr. Tanja Hochstrasser

Dekan: Prof. Dr. med. Thomas Gudermann

Tag der mündlichen Prüfung: 02.12.2021

Dedicated to my parents and sister, and in loving memory of Lilo and Lothar.

Affidavit

	LUDWIG- MAXIMILIANS- UNIVERSITÄT MÜNCHEN	Promotionsbüro Medizinische Fakultät		
Eidesstattliche Versicherung				

Rühling, Sebastian

Name, Vorname

Ich erkläre hiermit an Eides statt, dass ich die vorliegende Dissertation mit dem Titel:

Neurodegeneration in multiple sclerosis mouse models

selbständig verfasst, mich außer der angegebenen keiner weiteren Hilfsmittel bedient und alle Erkenntnisse, die aus dem Schrifttum ganz oder annähernd übernommen sind, als solche kenntlich gemacht und nach ihrer Herkunft unter Bezeichnung der Fundstelle einzeln nachgewiesen habe.

Ich erkläre des Weiteren, dass die hier vorgelegte Dissertation nicht in gleicher oder in ähnlicher Form bei einer anderen Stelle zur Erlangung eines akademischen Grades eingereicht wurde.

München, 03.12.2021

Ort, Datum

Sebastian Rühling

Unterschrift Doktorandin bzw. Doktorand

Table of Contents

Affidavit	5
Table of Contents.....	6
List of abbreviations	7
List of publications.....	9
1. Introduction.....	10
1.1 Multiple sclerosis.....	10
1.2 Clinical and neuropathological features of progressive MS.....	13
1.3 The cuprizone animal model.....	15
1.4 Aim of the thesis (paper I)	17
1.5 Aim of the thesis (paper II).....	18
2. Contribution to the publications	20
2.1 Contribution to paper I: <i>Visualization of the Breakdown of the Axonal Transport Machinery: A Comparative Ultrastructural and Immunohistochemical Approach</i> *	20
2.2 Contribution to paper II: <i>Stereological Investigation of Regional Brain Volumes after Acute and Chronic Cuprizone-Induced Demyelination</i> **	21
3. Summary (English).....	22
4. Summary (Deutsch)	23
5. Paper I.....	25
6. Paper II.....	41
7. References.....	59

List of abbreviations

APC	adenomatous polyposis coli
APCs	antigen-presenting cells
APP	amyloid-precursor-protein
BBB	blood-brain barrier
CIS	clinically isolated syndrome
CNS	central nervous system
COX4	cytochrome c oxidase subunit 4
DAWN	diffusely-abnormal white matter
DMTs	disease modifying therapies
EAE	experimental autoimmune encephalomyelitis
EDSS	expanded disability status scale
EM	electron microscopy
GFAP	glial fibrillary acidic protein
GWAS	genome-wide association studies
HLA	human leukocyte antigen
IBA1	ionized calcium-binding adaptor molecule 1
MS	multiple sclerosis
NAGM	normal-appearing gray matter
NAWM	normal-appearing white matter
OLs	oligodendrocytes
OR	odds ratio
PLP	anti-proteolipid protein
PPMS	primary-progressive multiple sclerosis
RIS	radiologically isolated syndrome

RRMS	relapsing-remitting multiple sclerosis
SNPs	single-nucleotide polymorphisms
SPMS	secondary-progressive multiple sclerosis
vGLUT1	vesicular glutamate transporter 1
18F-FDG PET	[18F]-fluoro-2-deoxy-d-glucose positron-emission tomography

List of publications

Published work conducted during the thesis that is used for the cumulative dissertation

- I. **Rühling, S.**, Kramer, F., Schmutz, S., Amor, S., Jiangshan, Z., Schmitz, C., ... & Hochstrasser, T. (2019). Visualization of the breakdown of the axonal transport machinery: a comparative ultrastructural and immunohistochemical approach. *Molecular neurobiology*, 56(6), 3984-3998.
<https://doi.org/10.1007/s12035-018-1353-9>
- II. Hochstrasser, T., **Rühling, S.**, Hecher, K., Fabisch, K. H., Chrzanowski, U., Brendel, M., ... & Kipp, M. (2019). Stereological investigation of regional brain volumes after acute and chronic cuprizone-induced demyelination. *Cells*, 8(9), 1024.
<https://doi.org/10.3390/cells8091024>

Additional work conducted and published during the thesis that is not used for the cumulative dissertation

- III. Hochstrasser, T., Jiangshan, Z., **Rühling, S.**, Schmitz, C., & Kipp, M. (2018). Do pre-clinical multiple sclerosis models allow us to measure neurodegeneration and clinical progression? *Expert review of neurotherapeutics*, 18(5),351-353.
<https://doi.org/10.1080/14737175.2018.1459190>
- IV. Zhan, J., Yakimov, V., **Rühling, S.**, Fischbach, F., Nikolova, E., Joost, S., ... & Kipp, M. (2019). High speed ventral plane videography as a convenient tool to quantify motor deficits during pre-clinical experimental autoimmune encephalomyelitis. *Cells*, 8(11), 1439.
<https://doi.org/10.3390/cells8111439>
- V. Zhan, J., Fegg, F. N., Kaddatz, H., **Rühling, S.**, Frenz, J., Denecke, B., ... & Kipp, M. (2021). Focal white matter lesions induce long-lasting axonal degeneration, neuroinflammation and behavioral deficits. *Neurobiology of Disease*, 105371.
<https://doi.org/10.1016/j.nbd.2021.105371>

1. Introduction

1.1 Multiple sclerosis

Multiple sclerosis (MS) is a chronic inflammatory disease of the central nervous system (CNS) with profound demyelination and neurodegeneration that leads to long-term disability in most patients. It is estimated that more than 2.8 million people live with MS worldwide. In high prevalence countries, 1 in 300 people is diagnosed with the disease (1). MS predominantly affects individuals in their early adult life and shows a relatively high female-to-male ratio (~2–3:1) (2).

Although MS can follow a heterogeneous clinical pattern over time (i.e., attacks, exacerbations, periods of clinical stability), three main clinical subtypes have been described (3). Initially, around 85% of patients show a biphasic course called relapsing-remitting multiple sclerosis (RRMS). This phase is characterized by acute neurological deterioration (relapses), followed by a partial or complete recovery and episodes of clinical stability (remission) (4). Symptoms may include sudden visual impairment, sensorimotor disability, pain and neurocognitive impairment, depending on the location of the inflammatory lesion. At later stages, progression of neurological disability with or without occasional relapses is observed in ~90% of patients initially diagnosed with RRMS (4). This distinct course is termed secondary-progressive multiple sclerosis (SPMS), in which minor remissions and plateaus can occur. A minority of ~10-15% of patients present with a nearly steady progression of neurological deterioration from onset, with or without minor fluctuations but no relapses. This clinical course is commonly referred to as primary-progressive multiple sclerosis (MS) (5).

Despite tremendous research efforts, the ultimate cause of MS remains unknown. However, underlying genetic and environmental factors are becoming better understood (6). Various migration studies have shown that, at least to some extent, geographic factors contribute to the disease risk in early life (7–9). The likelihood of developing MS is positively correlated with increasing distance from the equator. In addition, a young age at migration is associated with the risk of the new environment, whereas migration after adolescence does not change the environmental risk. Other well-established environmental and lifestyle factors

that increase the risk of developing MS include smoking, EBV seropositivity, adolescent obesity, and low Vitamin D levels (6). Some of these factors interact with the human leukocyte antigen (HLA) complex, a region on human chromosome 6. This region contains ~200 genes that encode for proteins with crucial roles in the immune system. In particular, HLA class II is relevant for antigen binding and presentation to CD4⁺ T_H-cells, while HLA class I is important for antigen presentation to CD8⁺ cytotoxic T-cells. The class II allele HLA-DRB1*15:01, for example, is strongly associated with an increased risk of disease (OR ~3) (10). Taken together, genetic and environmental factors, in combination with potentially modifiable lifestyle factors, play an important but not exclusive role in the etiology of MS.

Although the trigger(s) of the initial immune response remains unclear, yet two opposing hypotheses exist as to how this event might be initiated. First, the outside-in hypothesis states that the initial event takes place outside the CNS (e.g., in the event of a systemic infection) where extrinsic antigens trigger the activation of the immune system. Molecular mimicry, direct cross activity, and bystander activation have been proposed as mechanisms that could lead to the activation of autoreactive T-cells that eventually cross the blood-brain barrier (BBB) (11). Upon arrival in the previously unaffected CNS, the release of cytokines promotes inflammation, permeability of the BBB and recruitment of other immune cells, i.e., plasma cells and monocytes, to invade the CNS. To date, however, no immune response or antigen that is specific for MS has been found (12).

Second and in contrast, the inside-out model proposes that intrinsic CNS events play a key role in the initiation process (13,14). According to this hypothesis, cyto-degenerative events, particularly oligodendrocyte destruction or myelin pathology, lead to a release of highly autoantigenic CNS components into the periphery, triggering a predisposed immune system (15). In fact, oligodendrocyte destruction was found in autopsy tissues during early lesion development when T-cells are virtually absent (16). Many authors argue that there is no direct pathway between the CNS and the adaptive immune system, thus making this hypothesis unlikely. However, various pathways for antigen leakage have now

been described, e.g. drainage into deep cervical lymph nodes, direct involvement of antigen-presenting cells (APCs), and the hypothesis of antigen drainage via the cerebrospinal fluid, termed the glymphatic system (17–19). In addition, recent studies using animal models have shown that the degeneration of oligodendrocytes can drive immune cell recruitment into the CNS and subsequent lesion formation (20,21). Whatever the initial trigger, both pathways share common histopathological endpoints –demyelination, gliosis and acute neuroaxonal damage –, which lead to further recruitment of peripheral immune cells into the CNS.

During an acute relapse, in particular, focal immune-mediated white matter demyelination but also edema formation lead to decreased neuronal integrity and axonal dysfunction (22,23). The immediate consequences of acute demyelination have been studied in detail. Damage to the myelin insulation layer results in complete or intermitted conduction blocks, as the main function of the myelin sheath is to facilitate the conduction of electrical impulses along the axons. For example, visual loss in typical opticus neuritis is caused by a conduction block (24). Initially, the CNS employs various mechanisms to cope with tissue damage. Thus, after demyelination, the axonal membrane undergoes several changes, such as re-distribution of sodium channels and remyelination (25–27). Such mechanisms allow some axons to recover and at least partially restore nerve conduction, thus contributing to relapse recovery (28). In a secondary process, neuroplasticity, i.e., the reorganization of cortical representations and long-term potentiation at the synaptic level, is thought to compensate for tissue damage (29,30). However, after a period of ~10-15 years, the compensatory capacity of the CNS is exceeded, and the accumulated residual damage becomes apparent through changes in clinical presentation and increasing neurological deficits. At this point, patients have entered the progressive stage.

1.2 Clinical and neuropathological features of progressive MS

Profound focal inflammation and involvement of the peripheral immune system are currently thought to be the main drivers of the relapse-remitting phase. In contrast, different pathomechanisms are hypothesized to drive disease progression during the progressive disease states. This hypothesis is supported by several arguments.

First, the clinical course undergoes remarkable changes after the switch from RRMS to SPMS. The frequency of clinically detectable relapses decreases significantly, indicating reduced activity of the adaptive immune system (see Fig. 1) (31). In contrast to RRMS, SPMS is associated with a progressive, irreversible neurological decline and brain atrophy, independent of exacerbations and remissions. Neuroimaging studies that have examined these long-term effects in SPMS have shown only a modest correlation between the extend of early inflammation and brain or spinal cord atrophy (32,33). In addition, patients without disease activity during the first two years after diagnosis, and thus with little peripheral-driven inflammation, had no difference in long-term outcome compared to the overall cohort (34). Taken together, these findings suggest that there are additional pathomechanisms that are most apparent in later stages of MS (35).

Second, currently available pharmacotherapeutics have shown tremendous efficacy in reducing relapses and neuroinflammation. However, despite their vast utility during the early phases of the disease, anti-inflammatory and immunomodulatory therapeutics are largely ineffective in the progressive stages (i.e., SPMS and PPMS) (36). Of note, one of the most widely used disease-modifying therapies (DMTs), i.e., Interferon β , does not delay permanent disability, although it significantly reduces relapse activity (37). One explanation for the failure of DMTs during the progressive phase is that immune responses in the later phases may be confined to the CNS compartment. This could subsequently create a microenvironment that potentially supports brain resident immune cells, rendering DMTs ineffective (38). Remarkably, the sphingosine 1-phosphate receptor modulator siponimod (Mayzent®) not only reduces inflammatory activity, but also interferes directly with brain cells, potentially reducing neurodegeneration and brain atrophy (39). In 2019, siponimod became the first drug to be approved for the treatment of SPMS (40).

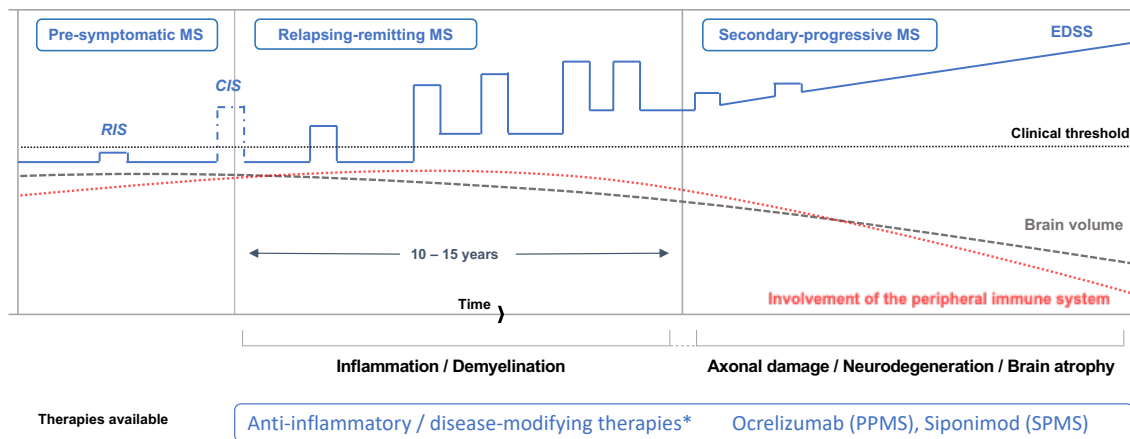


Figure 1: Schematic illustration of the course of multiple sclerosis (MS). Inflammation occurs in the pre-symptomatic phase, but the threshold level for clinical symptoms is not reached. In cases where an MRI scan is performed, early white matter lesions may be seen, and the condition is termed radiological isolated syndrome (RIS). When a patient presents with the first neurological episode while not yet firmly meeting the McDonald criteria, the condition is defined as clinically isolated syndrome (CIS). CIS often, but not always, transitions into MS. The relapsing-remitting (RR) phase is associated with acute neurological deterioration, followed by partial or complete recovery. In secondary-progressive MS (SPMS), the contribution of the peripheral immune system diminishes while clinical disability worsens irreversibly. In the later stages of MS, whole brain atrophy is observed. To date, only two disease modifying therapies (DMTs) have been approved for progressive disease phases (i.e., Ocrelizumab and Siponimod). *Number of disease-modifying drugs = 14. Blue line: Clinical disability displayed as expanded disability status scale (EDSS). Black dotted line: clinical threshold. Gray dotted line: evolution of brain volume over time. Red dotted line: involvement of the peripheral immune system. Illustration based on (11).

Third, on the histopathological level, actively demyelinating plaques become less prominent and the amount of infiltrating T-cells decreases during the progressive phase (41). Instead, studies that have carefully examined human brain tissue have found diffusely-abnormal white matter (DAWN) to harbor the characteristics of classic neurodegeneration. Interestingly, these areas showed no acute axonal pathology, blood-brain barrier leakage or reactive inflammation (42). In addition, regions of so called normal-appearing white matter (NAWM) and normal-appearing gray matter (NAGM) have been discovered. They are termed “normal-appearing” because they present normal on routine myelin stains, such as anti-proteolipid protein (PLP). These regions, distant from focal areas of inflammation, show brain damage and axonal pathology with little peripheral immune cell involvement (43,44). Instead, histopathological characteristics include diffuse

gliosis, microglial activation, and most notably, axonal loss (22,23,41). Thus, neurodegeneration could be driven, at least in part, by brain resident immune cells (45,46).

In conclusion, it is believed that peripheral driven inflammation is not the primary driver for ongoing tissue injury and accumulating disability. Instead, different neurodegenerative pathomechanisms in white matter and gray matter are predominant events leading to neuroaxonal loss. These events could act together with ongoing inflammation. Neuroaxonal loss, i.e., neurodegeneration, is therefore widely believed to be the fundamental pathological substrate of clinical disability (14,22,43,47,48). However, the specific molecular mechanisms driving ongoing axonal damage and subsequent neurodegeneration are poorly understood and, thus, remain to be investigated in the future.

1.3 The cuprizone animal model

Various animal models (e.g., rats, mice and marmosets) are available to study CNS disease mechanisms. It is important to mention that a perfect animal model does not exist. With respect to MS, this is primarily due to the fact that MS is a purely human disease that does not occur in animals. Moreover, MS shows a highly heterogeneous course in terms of clinical and neuropathological aspects. Yet, animal models allow us to study certain aspects of the disease. For example, the experimental autoimmune encephalomyelitis (EAE) model is the most common model to study CNS inflammation and T cell-dependent pathology and has greatly contributed to our knowledge of the relapsing-remitting phase (49). Many DMTs, e.g. natalizumab (Tysabri), were initially successfully tested in preclinical studies in the EAE model (50). However, the EAE model alone poorly reflects neurodegenerative features and therefore cannot be used to address the progressive phase.

A widely used animal model that can provide insight into the mechanisms of neurodegeneration in MS is the cuprizone model. In this model, rodents are usually fed with normal chow and 0.25% cuprizone (Biscyclohexanone oxaldihydrazone), a selective copper chelator that was first described by Gustav

Nilsson in 1950 (51). The animal model was introduced in the 1960s by William W. Carlton. He noticed that cuprizone administration leads to the formation of CNS lesions, microglial activation and development of hydrocephalus in rodents (52,53). Although the complex mechanisms have not been fully revealed, cuprizone is thought to alter the respiratory chain in mitochondria that require copper as a co-factor. Mitochondria of mature oligodendrocytes (OLs) are particularly vulnerable to metabolic impairment. As a consequence, cuprizone intoxication results in oxidative stress, profound loss of mature OLs, activation of microglia and astrocytes, and finally profound demyelination (54). Importantly, in contrast to EAE, T-cells play a non-dominant role in this model and neurodegeneration can be studied independently of peripheral immune system driven inflammation (55,56). In addition, BBB breakdown, which is a hallmark during acute lesion formation, is not or just minor present in the cuprizone model (57). A major feature of the cuprizone model is the highly reproducible demyelination of the white matter track corpus callosum (CC). Previously, it was assumed that predominantly the CC is affected. However, recent studies have demonstrated that other brain areas (internal capsule, the thalamus, hippocampus, anterior commissure, and cerebellar peduncles) are also markedly affected (58–60). Of note, lesions also appear within areas of gray matter, in particular in the cortex (61). After a cuprizone intoxication period of 5 weeks, a so-called acute demyelination phase is reached and demyelination is complete (55). White matter tracts display axonal injury, and a positive correlation between the extend of axonal damage and microglial activation has been described (62,63). If the cuprizone diet is withdrawn after this period, extensive remyelination occurs (55). Subgroups of early MS lesions exhibit similar patterns of de- and remyelination, thus the cuprizone model has been extensively used to study the dynamics underlying demyelination (64–66). When cuprizone treatment is prolonged to 12-13 weeks, the mechanisms leading to remyelination are severely altered, oligodendrocyte regeneration is impaired, and chronic demyelinated lesions and persistent axonal damage is induced (67).

Thus, in summary, important characteristics of progressive MS are well recapitulated by the cuprizone model, namely de- and remyelination, and subsequent damage to the neuroaxonal unit (63,67).

1.4 Aim of the thesis (paper I)

The first publication investigated the complex nature of axonal damage in the cuprizone animal model of MS. Intact axonal transport is vital for neuronal health, and impairment to this vulnerable target can contribute to axon degeneration (68). Acute axonal injury is most frequently quantified by immunohistochemical staining against amyloid precursor protein (APP), an integral glycoprotein type 1 that is transported to the axon terminal *via* fast anterograde transport (23,43,69). There, APP is thought to play a crucial role in synaptic maintenance and neuroaxonal health (70,71). Normal levels of APP are undetectable by immunohistochemistry. However, when axonal transport is disturbed, APP accumulates at sites of axonal injury, forming detectable spheroid-like swellings.

To obtain an accurate picture of the complex dynamics of axonal damage, precise measurement methods are essential. Therefore, we compared current gold-standard methods, i.e., immunohistochemistry and serial block-face scanning electron microscopy (3D EM), to investigate whether they can truly reflect axonal pathology. By comparing the volumes of cuprizone induced APP⁺ spheroids in the CC using both methods, we demonstrated that spheroid volume determined by immunohistochemistry correlates well with the ultrastructural morphology. We then hypothesized that impairment of axonal transport of other vesicles and organelles (e.g., mitochondria) could also be accurately visualized by immunohistochemistry. In that context, we investigated whether immunohistochemical detection of these transport deficits could potentially serve as new markers of axonal damage. Among others, transport cargos of the vesicular glutamate transporter 1 (vGLUT1) and cytochrome c oxidase subunit 4 (COX4) accumulated in demyelinated areas. Increased numbers of spheroids were observed after acute demyelination. After chronic demyelination, spheroids were still observable, albeit to a lower extent. In co-localization experiments, the new candidate proteins were compared to the current gold-standard staining against APP. There, vGLUT1 and COX4 co-localized well with APP after acute and chronic demyelination. In immunofluorescence experiments, we confirmed that vGLUT1 and COX4 did not colocalize with astrocytes, mature oligodendrocytes or microglia. To test the relevance of our results, we applied the

markers in human tissue of MS patients. Here, synaptic and mitochondrial spheroids were found as well.

1.5 Aim of the thesis (paper II)

For many years, MS was considered to be a purely white matter disease. In the recent decades, it has become evident that gray matter pathology is also an essential aspect of the underlying pathology (72–74). In fact, the phenomenon was described in MS brains as early as the 1960s (74,75). Brain atrophy appears to occur not only in the late progressive phase but also in the earliest stages of the disease (76). Whole brain, gray matter, and white matter volume loss is the visible *in vivo* substrate of neurodegeneration (75). Quantitative MRI has been found promising to monitor neurodegeneration (32,75), and brain volume loss correlates robustly with the extent of clinical disability progression (77). A substantial number of clinical trials have now frequently used whole brain atrophy as a key outcome measurement (78). Thus, studying the underlying mechanisms leading to brain atrophy could help to develop new targets to postpone or prevent long-term disability (79,80). However, with regard to preclinical studies, brain atrophy in MS has not been a focused area simply due to the lack of suitable animal models.

Hence, the second publication aimed to investigate whether brain volume and neuroaxonal loss can be reliably studied in different phases of the cuprizone model. We studied cortical, subcortical, and callosal volumes by design-based stereological analysis after acute and chronic cuprizone-induced demyelination (81). After 5 weeks (acute phase), all brain areas examined had volumes comparable to controls despite extensive demyelination and profound axonal damage. This could be due to the fact that (a) acute demyelination does not induce brain volume loss or (b) cuprizone induces changes, e.g., microglial activation, that mask the volume loss. In the chronic demyelination period with ongoing microgliosis, however, significant whole brain volume loss was observed. This could, at least in part, be indicative of true tissue loss. With regard to discrete subcortical areas, we found a significant volume reduction to be present in the thalamus and internal capsule. The thalamus forms the largest part of the diencephalon and is highly interconnected with many other brain areas.

There is strong evidence from clinical and histological studies that the thalamus is integrally involved in the pathological process of MS (82). Indeed, the thalamic volume has been identified as a strong predictor for cognitive decline in MS patients (83) and additionally correlates with the EDSS score (84). Interestingly, in our study, thalamic volume loss was paralleled by glucose hypermetabolism as measured by ^{18}F -FDG PET. Of note, the cortex volume remained unaffected by chronic demyelination.

To investigate whether the volume loss was due to true neuronal loss, we quantified the neuronal densities and total number of neurons in the cerebral cortex and in the entire subcortical area. In all subcortical areas as well as in the cortex, density and number of neurons were comparable to the control group. If the pathological substrate of volume loss in the cuprizone model is not due to loss from neurons, axonal degeneration may be one possible explanation. In areas of profound volume loss, i.e., in the thalamus and internal capsule, we found numerous APP⁺ spheroids, indicating axonal damage. Other plausible mechanisms could include loss of myelin, oligodendrocyte or astrocyte degeneration, and synaptic pathology.

2. Contribution to the publications

2.1 Contribution to paper I: *Visualization of the Breakdown of the Axonal Transport Machinery: A Comparative Ultrastructural and Immunohistochemical Approach**

1. Conceptualization and study design in consultation with supervisors
2. Animal care of C57BL/6 mice
3. Tissue preparation
 - 3.1. Animal perfusion and post-fixation
 - 3.2. Paraffin embedding
 - 3.3. Sectioning of paraffin-embedded tissue
 - 3.4. Cryofixation
 - 3.5. Cryo-sectioning
 - 3.6. Microscopic evaluation of human brain autopsy samples
4. Histochemistry
 - 4.1. Immunohistochemistry staining
 - 4.2. Immunofluorescence staining
5. Microscopic imaging
 - 5.1. Light sheet fluorescence microscopy
 - 5.2. Immunofluorescence microscopy
6. Data quantification and interpretation
 - 6.1. Stereology
 - 6.2. Visual image analysis
 - 6.3. Immunohistochemical analysis
 - 6.4. Volume analysis
 - 6.5. Densitometric analysis
7. Statistical analysis
8. Manuscript
 - 8.1. Figure preparation
 - 8.2. Manuscript writing

* Contribution as first author. No shared first authorship was applied.

2.2 Contribution to paper II: *Stereological Investigation of Regional Brain Volumes after Acute and Chronic Cuprizone-Induced Demyelination***

1. Study design in consultation with supervisors
2. Microscopic imaging
 - 2.1. Light sheet fluorescence microscopy
3. Histochemistry
 - 3.1. Free-floating immunofluorescence
4. Neuroimaging
 - 4.1. Assistance in [18F]-Fluoro-2-deoxy-d-glucose Positron-Emission Tomography (FDG PET) Imaging
5. Data quantification and interpretation
 - 5.1. Stereology
6. Manuscript
 - 6.1. Figure preparation
 - 6.2. Manuscript writing – review and editing

**Contribution as second author.

3. Summary (English)

Multiple sclerosis harbors closely related destructive hallmarks, namely acute damage to the neuroaxonal unit, progressive neuroaxonal degeneration and brain atrophy. In addition to other established underlying mechanisms of MS, such as focal inflammation, these interrelated pathological processes have been identified as one of the major contributors to long-term disability, particularly in the chronic stages of the disease. The main goal of MS therapy is to delay or prevent such accumulation of disability. Although our knowledge has advanced considerably, treatment options to prevent progression of the disease in chronic stages are still limited. Therefore, a better understanding of the underlying mechanisms leading to neuroaxonal damage and subsequent neuroaxonal loss is needed.

In this study, we hypothesized that neuroaxonal pathology can be investigated in the acute and chronic phases of the cuprizone model. After treatment of male C57BL/6J mice with 0.25% cuprizone, we analyzed the accumulation of anterograde transport cargos, brain volume and neuronal loss using current gold-standard methods, i.e., immunohistochemistry, immunofluorescence microscopy, 3D EM, ^{18}F -FDG PET, and design-based stereology.

In the two publications presented, we provided evidence that the cuprizone model is suitable to study neurodegenerative aspects of MS. We demonstrated that chronic but not acute cuprizone-induced demyelination leads to significant subcortical atrophy, although this is presumably not due to neuronal loss. Furthermore, we identified the thalamus and internal capsule as the most vulnerable regions for volumetric changes. Thus, the cuprizone model may be an appropriate tool when addressing subcortical brain volume loss. To investigate the precise pathomechanisms causing axonal injury, we demonstrated that 3D EM microscopy combined with immunohistochemistry is a reliable study tool. Our data showed the accumulation of distinct vesicular and mitochondrial vesicles at sites of acute and chronic axonal injury. Here, vGLUT1 and COX4 colocalized with APP and did not show cross-reactivity with oligodendrocytes, astrocytes, or microglia. We further validated our findings in human MS lesions in post-mortem tissue. Thus, we can conclude that vGLUT1 and COX4 serve as reliable markers for acute and chronic axonal damage in the human central nervous system.

4. Summary (Deutsch)

Die Multiple Sklerose weist eng miteinander verbundene destruktive Merkmale auf, im Einzelnen, die akute Schädigung der neuroaxonalen Einheit, progrediente neuroaxonale Degeneration und Hirnatrophie. Neben anderen bekannten Mechanismen der MS, wie z.B. fokale Inflammation, wurden diese zusammenhängenden pathologischen Prozesse als einer der Hauptfaktoren für langfristige klinische Behinderung identifiziert, insbesondere in den chronischen Stadien der Erkrankung. Das Hauptziel der MS-Therapie ist es, eine Akkumulation dauerhafter Behinderungen zu verzögern oder zu verhindern. Obwohl unser Verständnis erhebliche Fortschritte gemacht hat, sind die Behandlungsmöglichkeiten, die das Fortschreiten der Erkrankung in den chronischen Stadien verhindern, immer noch begrenzt. Daher ist ein besseres Verständnis der zugrundeliegenden Mechanismen, welche zur neuroaxonalen Schädigung und nachfolgend zum neuroaxonalen Verlust führen, erforderlich.

In dieser Studie stellten wir die Hypothese auf, dass die neuroaxonale Pathologie in den akuten und chronischen Phasen des Cuprizin-Modells untersucht werden kann. Nach der Behandlung von männlichen C57BL/6J-Mäusen mit 0,25% Cuprizin analysierten wir die Akkumulation von anterograden Transport-Cargos, das Hirnvolumen und den neuronalen Verlust mit Hilfe gängiger Gold-Standard-Methoden (Immunfluoreszenzmikroskopie, 3D-Elektronenmikroskopie, ^{18}F -FDG-PET und design-basierter Stereologie).

In den beiden vorgestellten Publikationen konnten wir nachweisen, dass das Cuprizin-Modell geeignet ist, neurodegenerative Aspekte der MS zu untersuchen. Wir konnten zeigen, dass eine chronische, nicht aber eine akute Cuprizin-induzierte Demyelinisierung zu einer signifikanten subkortikalen Atrophie führt, obwohl diese vermutlich nicht auf einen neuronalen Verlust zurückzuführen ist. Außerdem identifizierten wir den Thalamus und die Capsula interna als die am meisten vulnerablen Regionen für volumetrische Veränderungen. Somit könnte das Cuprizin-Modell eine geeignete Methode sein, um den subkortikalen Hirnvolumenverlust zu untersuchen. Wir konnten zeigen, dass die 3D-Elektronenmikroskopie in Kombination mit Immunhistochemie ein zuverlässiges Untersuchungsinstrument ist, um die genauen Pathomechanismen zu untersuchen, welche der axonale Schädigung zugrunde liegen. Unsere Daten zeigten die Akkumulation verschiedener

vesikulärer und mitochondrialer Vesikel an Stellen akuter und chronischer axonaler Schädigung. Hier ko-lokalisierten vGLUT1 und COX4 mit APP und zeigten keine Kreuzreaktivität mit Oligodendrozyten, Astrozyten oder Mikroglia. Darüber hinaus konnten wir unsere Ergebnisse in MS-Läsionen in humanem *post mortem* Hirngewebe validieren. Zusammenfassend können wir daher schließen, dass vGLUT1 und COX4 zuverlässige Marker für akute und chronische axonale Schädigung im menschlichen Zentralnervensystem sind.

5. Paper I

Rühling S, Kramer F, Schmutz S, Amor S, Jiangshan Z, Schmitz C, Kipp M, Hochstrasser T. Visualization of the Breakdown of the Axonal Transport Machinery: a Comparative Ultrastructural and Immunohistochemical Approach. *Mol Neurobiol.* 2019 Jun;56(6):3984-3998. doi: 10.1007/s12035-018-1353-9. Epub 2018 Sep 21. PMID: 30238390.



Visualization of the Breakdown of the Axonal Transport Machinery: a Comparative Ultrastructural and Immunohistochemical Approach

Sebastian Rühling¹ · Franziska Kramer¹ · Selina Schmutz¹ · Sandra Amor^{2,3} · Zhan Jiangshan¹ · Christoph Schmitz¹ · Markus Kipp¹ · Tanja Hochstrasser¹

Received: 25 June 2018 / Accepted: 13 September 2018 / Published online: 21 September 2018
 © Springer Science+Business Media, LLC, part of Springer Nature 2018

Abstract

Axonal damage is a major factor contributing to disease progression in multiple sclerosis (MS) patients. On the histological level, acute axonal injury is most frequently analyzed by anti-amyloid precursor protein immunohistochemistry. To what extent this method truly detects axonal injury, and whether other proteins and organelles are as well subjected to axonal transport deficits in demyelinated tissues is not known. The aim of this study was to correlate ultrastructural morphology with the immunohistochemical appearance of acute axonal injury in a model of toxin-induced oligodendrocyte degeneration. C57BL/6J mice were intoxicated with 0.25% cuprizone to induce demyelination. The corpus callosum was investigated by serial block-face scanning electron microscopy (i.e., 3D EM), immunohistochemistry, and immunofluorescence microscopy. Brain tissues of progressive MS patients were included to test the relevance of our findings in mice for MS. Volumes of axonal swellings, determined by 3D EM, were comparable to volumes of axonal spheroids, determined by anti-APP immunofluorescence stains. Axonal swellings were present at myelinated and non-myelinated axonal internodes. Densities of amyloid precursor protein (APP)⁺ spheroids were highest during active demyelination. Besides APP, vesicular glutamate transporter 1 and mitochondrial proteins accumulated at sites of axonal spheroids. Such accumulations were found as well in lesions of progressive MS patients. In this correlative ultrastructural-immunohistochemical study, we provide strong evidence that breakdown of the axonal transport machinery results in focal accumulations of mitochondria and different synaptic proteins. We provide new marker proteins to visualize acute axonal injury, which helps to further understand the complex nature of axonal damage in progressive MS.

Keywords Cuprizone · Axonal damage · APP · VGLUT1 · Mitochondria

Introduction

There is broad consensus that multiple sclerosis (MS) represents more than a purely inflammatory demyelinating disease. Most patients initially show with a relapsing-remitting (RR) course, which is usually followed by a secondary progressive phase [1]. These clinical phenotypes are thought to be

associated with different underlying pathologies. While inflammatory lesions in the white matter are believed to be associated with the relapses during the RR disease stage, neuronal loss and axonal damage are widely considered to underlay the disease progression [2, 3]. Morphological changes of injured axons include focal axonal swellings, which are associated with impaired axonal transport of proteins and organelles. This impaired axonal transport machinery can be visualized by immunohistochemistry for accumulated proteins that are synthesized in the cell body and transported along the axon to their synaptic destination [4–7]. The most commonly used immunohistochemical marker to visualize axonal transport deficits is amyloid precursor protein (APP) [7]. APP is an integral glycoprotein type 1, which is transported to the axonal terminal via anterograde axonal transport [8]. There, APP is considered to regulate synaptic activity and stability [9, 10]. In case of a disturbed axonal transport machinery, APP accumulates at the side of axon injury and can then be visualized by immunohistochemistry as spheroids [11, 12]. Focal accumulation of APP is observed in MS lesions and

Electronic supplementary material The online version of this article (<https://doi.org/10.1007/s12035-018-1353-9>) contains supplementary material, which is available to authorized users.

✉ Tanja Hochstrasser
 tanja.hochstrasser@med.uni-muenchen.de

¹ Department of Neuroanatomy, Ludwig-Maximilians-University of Munich, Pettenkofenstr. 11, 80336 Munich, Germany

² Department of Pathology, VU University Medical Center, Amsterdam, The Netherlands

³ Blizard Institute, Barts and The London School of Medicine and Dentistry, Queen Mary University of London, London, UK

correlates with densities of macrophages and CD8⁺ T lymphocytes within lesions [13, 14]. The accumulation of APP⁺ spheroids has also been observed in animal models of MS, including the cuprizone model [15].

The cuprizone model is a model of toxic demyelination. Oral administration of cuprizone induces degeneration of oligodendrocytes, which is closely followed by microglia and astrocyte activation that ultimately leads to demyelination [16, 17]. After 5–6 weeks of cuprizone intoxication, the corpus callosum is almost completely demyelinated, a process called “acute demyelination.” In contrast, prolonged cuprizone intoxication (> 12 weeks) leads to an impairment of oligodendrocyte regeneration and insufficient remyelination, termed “chronic demyelination” [18, 19]. Like in other preclinical MS animal models, in the cuprizone model, the number of APP⁺ spheroids correlates to the extent of inflammatory lesion activity [20].

For the maintenance of neuronal health and function, vesicular transport is vital [21, 22]. Vesicular glutamate transporters (VGLUTs) and the vesicular gamma-aminobutyric acid (GABA) transporter (VGAT) are specifically expressed in cell bodies and axon terminals of excitatory glutamatergic or inhibitory GABAergic and glycinergic neurons, respectively. They are transported from the cell body to nerve terminals via anterograde axonal transport. Then, they selectively move glutamate or GABA/glycine from the cytoplasm into synaptic vesicles and contribute via this mechanism to the maintenance of cell homeostasis [23, 24]. VGLUT1 is principally associated with excitatory cortico-cortical projections [25], while VGAT is expressed by inhibitory neurons [24].

Balanced mitochondrial transport is important for the maintenance of axonal health. Most mitochondria are generated in the cell body and are transported along the microtubular network by microtubule-based motor proteins to areas with high energy demands. Once an axon loses its myelin sheath (i.e., demyelination), the demand for energy increases [26] with subsequent changes in activity and density of mitochondria in demyelinated areas [27, 28]. Increased mitochondrial density is important for axon regeneration [28]; however, there is accumulating evidence that focal accumulation of axonal mitochondria may as well contribute to axonal degeneration [29].

The aim of this study was to correlate ultrastructural morphology with the immunohistochemical presentation of acute axonal injury in a model of toxin-induced oligodendrocyte degeneration.

Materials and Methods

Animals and Induction of Demyelination

C57BL/6J mice (Janvier Labs, Le Genest-Saint-Isle, France) and hGFAP/EGFP transgenic mice [30] were kept under

standard laboratory conditions according to the Federation of European Laboratory Animal Science Association’s recommendations. All experimental procedures were approved by the Review Board for the Care of Animal Subjects of the district government (Upper Bavaria, Germany, 55.2-1-54-2532-73-15) and were performed according to international guidelines on the use of laboratory mice. Demyelination was induced by feeding male mice (19–21 g) with ground standard rodent chow containing 0.25% (w/w) cuprizone (bis-cyclohexanone oxaldihydrazone, Sigma-Aldrich Inc.). Cuprizone treatment was maintained for 1, 3, 5, or 12 weeks. Control mice were fed standard rodent chow.

MS Tissue

Autopsy samples of human brain material were obtained from the Netherlands Brain Bank and with the ethical approval of the VU University Medical Ethical Committee (Amsterdam, The Netherlands). Paraffin-embedded post-mortem brain tissues were obtained through a rapid autopsy protocol from clinically and neuropathologically validated patients [31]. Studies were performed on postmortem human brain tissue from 4 MS cases (3 female, 1 male; 3 patients with SPMS, 1 patient with primary progressive MS). The ages of the patients ranged from 49 to 77 years. All patients had given written informed consent for autopsy and use of brain tissues for research purposes.

Immunohistochemistry (IHC) and Immunofluorescence

Mice were transcardially perfused with 3.7% paraformaldehyde in phosphate-buffered saline (PBS; pH 7.4). After overnight postfixation in the same fixative, brains were dissected, embedded in paraffin, and cut into 5- μ m-thick coronal or sagittal sections. Some brains were cryoprotected in sucrose, and thereafter quickly frozen. The frozen brains were cut into 40- μ m-thick coronal cryo-sections.

For immunohistochemistry, paraffin sections were deparaffinized, rehydrated, if necessary heat-unmasked in either citrate (pH 6.0) or Tris/EDTA-buffer (pH 9.0), and blocked with PBS containing 5% normal serum or a mixture of 2% normal serum, 0.1% cold water fish skin gelatin, 1% bovine serum albumin, and 0.05% Tween-20. Thereafter, slides were incubated overnight at 4 °C with the primary antibodies diluted in blocking solution. The following primary antibodies were used for mouse tissues: anti-myelin proteolipid protein (PLP; 1:5000, Bio-Rad; RRID:AB_2237198), anti-ionized calcium-binding adaptor molecule 1 (IBA1; 1:5000, Wako; RRID:AB_2665520), anti-glial fibrillary acidic protein (GFAP; 1:5000, Abcam; RRID:AB_304558), anti-amyloid precursor protein (APP; 1:5000; Merck Millipore;

RRID:AB_94882), anti-voltage-dependent anion-selective channel 1 (VDAC-1; 1:8000, Abcam; RRID:AB_443084), anti-cytochrome c oxidase subunit 4 (COX4; 1:500, Abcam; RRID:AB_445559), anti-vesicular glutamate transporter 1 (VGLUT1 1:2000; Abcam; RRID:AB_10710315), and anti-vesicular GABA amino acid transporter (VGAT; 1:1000, Thermo Fisher Scientific; RRID:AB_2637258). Sections were subsequently incubated with biotinylated secondary antibodies for 1 h at room temperature, followed by peroxidase-coupled avidin-biotin-complex (ABC kit; Vector Laboratories). The antigen-antibody conjugate was then visualized with 3,3'-diaminobenzidine (DAB; DAKO). Sections were counterstained with standard hematoxylin to visualize cell nuclei, if appropriate.

For immunofluorescence staining, slides were incubated with the following primary antibodies: anti-APP (1:5000), anti-VGLUT1 (1:2000), anti-adenomatous polyposis coli (APC, 1:200, Merck Millipore; RRID:AB_2057371), anti-IBA1 (1:2000), or anti-GFAP (1:5000) overnight at 4 °C. Sections were subsequently incubated with appropriate secondary antibodies (Alexa Fluor 488 or Alexa Fluor 594, 1:500, Invitrogen) for 2 h at room temperature and counterstained with 4',6-diamidino-2-phenylindole (DAPI). Frozen sections were stained free-floating (APP; 1:200).

To visualize myelin and inflammatory infiltrates in human tissues, anti-PLP (1:5000) and anti-major histocompatibility complex class II (MHC-II (LN3); 1:1500, Thermo Fisher Scientific; RRID:AB_10979984) antibodies were used. Axonal damage was detected by anti-APP (1:100), anti-VGLUT1 (1:2000) and anti-COX4 (1:500) antibodies. Antigen-primary antibody conjugates were visualized using horseradish peroxidase-labeled linked polymer secondary antibodies (EnVision, Dako) and DAB as a peroxidase substrate. For immunofluorescence staining, human tissues were incubated with the following primary antibodies: anti-APP (1:50) and anti-VGLUT1 (1:500) overnight at room temperature. Sections were subsequently incubated with appropriate secondary antibodies (Alexa Fluor 488 or Alexa Fluor 594, 1:500, Invitrogen) for 2 h at room temperature and counterstained with DAPI.

Serial Block-Face Scanning Electron Microscopy

Myelinated and partially demyelinated (i.e., 3 weeks cuprizone intoxication) corporacallosa (CC) tissues were analyzed by serial block-face scanning electron microscopy (i.e., 3D EM). To this end, mice were perfused with 2.5% (wt/vol) glutaraldehyde and 3.7% paraformaldehyde, and tissue blocks containing the CC were removed, stained with heavy metals, and embedded in resin as previously described (Ohno et al. 2014). 3D EM was performed by using a SigmaVP scanning electron microscope (Carl Zeiss) equipped with a 3View in-chamber ultramicrotome system (Gatan, Pleasanton, CA,

USA). Serial image sequences were generated at 80 nm steps, providing image stacks >10- μm deep and 48- μm \times 48- μm wide at a resolution of 5–10 nm per pixel. Images were processed with the software Reconstruct (BU, Boston, MA, USA) and BioVis3D (Montevideo, Uruguay). 3D EM was performed by Renovo Neural, Inc. (Cleveland, OH, USA).

Evaluation of Histological Parameters

A group of 3–8 animals was evaluated at each time point. The medial CC including the cingulum bundle (CB) was analyzed at the level R265 according to the online mouse brain atlas published by Sidman et al. (<http://www.hms.harvard.edu/research/brain/atlas.html>). Stained sections were analyzed using either a Nikon Eclipse 50i or an Olympus BX50 microscope. To determine levels of myelination, microgliosis, and astrocytosis in the region of interest (ROI), staining intensity was quantified using ImageJ (version 1.47v, NIH, Bethesda, MD, USA) as described previously [32, 33]. Staining intensities are given as percentage area of the entire ROI after binary conversion of the digital image. For quantification of APP⁺, VGLUT1⁺, COX4⁺, and VDAC1⁺ spheroid densities, particle densities of two consecutive sections per mouse were evaluated, averaged, and given as numbers of spheroids per mm². Spheroids were only counted if not localized around a cell nucleus. Additionally, the diameters of VGLUT1⁺ and COX4⁺ spheroids were measured using ImageJ after image calibration. For quantification of APP/VGLUT1 and APP/COX4 single and double positive spheroids, stained brain sections were digitalized, the CC outlined, and spheroids counted in a blinded approach using Stereo Investigator software (version 11, MBF Bioscience, Williston, VT, USA). Volume analysis of spheroids was done using 3D EM and confocal fluorescence image stacks. For fluorescence image stacks, serial image sequences from thick sections were generated at 200 nm steps using an Olympus BX51-Wi fluorescence microscope station and Stereo Investigator software. Images were processed and volumes of APP⁺ spheroids ($n = 90$) were automatically measured with NeuroLucida360 (version 2017.01.2, MBF Bioscience, Williston, VT, USA) and NeuroLucida Explorer software (version 2017, MBF Bioscience). In 3D EM image stacks, the areas of axonal swellings ($n = 20$) were measured using ImageJ and the volume was calculated using the formula: total area \times cutting thickness ($\cong 80$ nm). To compare the volumes of the two methods, the volume of cell nuclei was used as normalization value. The volume of cell nuclei was measured using NeuroLucida360/NeuroLucida Explorer ($n = 268$) and ImageJ ($n = 14$), respectively.

MS brain lesions were characterized by anti-MHC-II (LN3) and anti-PLP immunostainings as published previously [34]. To exclude autofluorescence of APP⁺/VGLUT1⁺ spheroids in MS lesions, double stained APP/VGLUT1 slides were compared with consecutive slides stained for APP only.

Statistical Analyses

All data are given as arithmetic means \pm standard error of the mean (SEM). Differences between groups were statistically tested using GraphPad Prism 5 (version 5.04, GraphPad Software Inc., La Jolla, CA, USA). In all cases, the Kolmogorov-Smirnov test was applied to test for normal distribution. To compare two groups, the Mann-Whitney *U* test was used for non-parametric data. To compare more than two groups, data were analyzed by one-way or two-way analysis of variance (ANOVA) followed by Bonferroni or Dunnett's *s* multiple comparison post hoc test. For analysis of non-parametric data the Kruskal–Wallis-test followed by Dunn's post hoc test was used. *p* values ≤ 0.05 were considered to be statistically significant and are indicated by asterisks or hashtags (*#*p* < 0.05; **###*p* < 0.01; ***####*p* < 0.001).

Results

Demyelination and Glial Activation During Cuprizone-Induced Demyelination

We first investigated the myelination status and glial activation during the course of cuprizone-induced demyelination (Fig. 1). Densitometrical analysis of anti-PLP immunoreactivity revealed normal myelin in the middle part of the CC and the CB of control mice. Severe demyelination of the CC, but not of the CB, was present after 5 weeks (acute demyelination) and 12 weeks (chronic demyelination) of cuprizone treatment (Fig. 1a–c, j). After acute demyelination, there was extensive infiltration of IBA1⁺ microglia and GFAP⁺ astrocytes that altered tissue morphology and increased the CC area. On the morphological level, microglia had retracted processes and enlarged cell bodies. Astrocytes, as well, showed enlarged cell bodies and disorganized process distribution. Notably, after chronic demyelination, IBA1 immunoreactivity was attenuated while severe astrocytosis was still present (Fig. 1d–i, k, l).

Ultrastructural Axonal Swellings Have a Similar Volume as Immunohistochemical Spheroids

It was shown that the magnitude of impaired axonal transport of proteins and organelles correlates with the extent of inflammatory demyelination [6, 7]. This impaired axonal transport is usually detected by immunohistochemistry against APP. In line with previous results [15, 20], APP⁺ spheroids were virtually absent in the CC of control animals (1.8 ± 1.3 APP⁺ spheroids/mm²; Fig. 2a), while profound accumulation of APP (454.3 ± 43.4 APP⁺ spheroids/mm²; *p* < 0.001 vs control) was detected after acute demyelination (5 weeks cuprizone) (Fig. 2b). APP⁺ spheroids were still observable at

week 12 (Fig. 2c), albeit to a lower extent (78.5 ± 14.5 APP⁺ spheroids/mm²; *p* < 0.001 vs control; *p* < 0.01 vs 5 weeks).

To further characterize axonal spheroids on the ultrastructural level, we performed 3D EM of the CC at week 3 and compared the ultrastructure with CC tissues isolated from control mice. Ultrastructural analysis revealed normal-shaped axons with intact myelin sheaths in control mice (Fig. 2d). In 3 weeks cuprizone-treated mice, axons were partly demyelinated and axonal swellings could be readily identified (Fig. 2e, f). Interestingly, we found axonal swellings affecting myelinated and demyelinated axonal internodes (Supplementary Fig. 1).

Although it seems reasonable that the axonal swellings observed on the ultrastructural level represent APP⁺ spheroids observed by immunofluorescence staining, this aspect was never proven experimentally. During tissue embedding, the true volumes of cells and cellular processes can change. To directly compare axonal swellings on the ultrastructural and histological level, first, the cell nuclei were reconstructed from confocal immunofluorescence and EM images and the volume of cell nuclei was measured (Fig. 2g, h). The volume of cell nuclei was larger in 3D EM images compared to cell nuclei in confocal immunofluorescence images (Fig. 2i), which could be due to tissue shrinkage or swelling. To correct for these artifacts in the subsequent analysis, the mean volume of cell nuclei of fluorescence images was divided by the mean volume of cell nuclei obtained from EM images, which resulted in a “normalization value” of 0.65. Second, the volume of axonal swellings was measured in consecutive EM images, and compared to the volume of axonal spheroids measured in free-floating brain sections processed for anti-APP immunofluorescence (Fig. 2j, k). To correct for tissue artifacts, values of ultrastructural axonal swellings (3D EM) were multiplied by the normalization value. As demonstrated in Fig. 2l, mean volumes of ultrastructural axonal swellings ($26.79 \mu\text{m}^3 \pm 7.20 \mu\text{m}^3$) did not significantly differ from mean volumes of APP⁺ spheroids ($31.32 \mu\text{m}^3 \pm 2.43 \mu\text{m}^3$) after correcting for tissue shrinkage or swelling artifacts.

Vesicular and Mitochondrial Proteins Accumulate as Spheroids

At higher resolution, it was evident that axonal swellings contained large numbers of two distinct densely packed structures, namely, (i) synaptic vesicles and (ii) mitochondria (Fig. 2f). Next, we wanted to analyze whether mitochondria, trapped in axonal swellings, can as well be visualized by immunohistochemistry. Furthermore, we asked whether synaptic vesicles, as observed by 3D EM, contain other synaptic proteins than APP. First, slides were processed for anti-VGLUT1 immunohistochemistry because the vast majority of cortical neurons are excitatory ones and release the excitatory transmitter glutamate. In the gray matter (i.e., cortex) of control and cuprizone-treated mice, VGLUT1 was

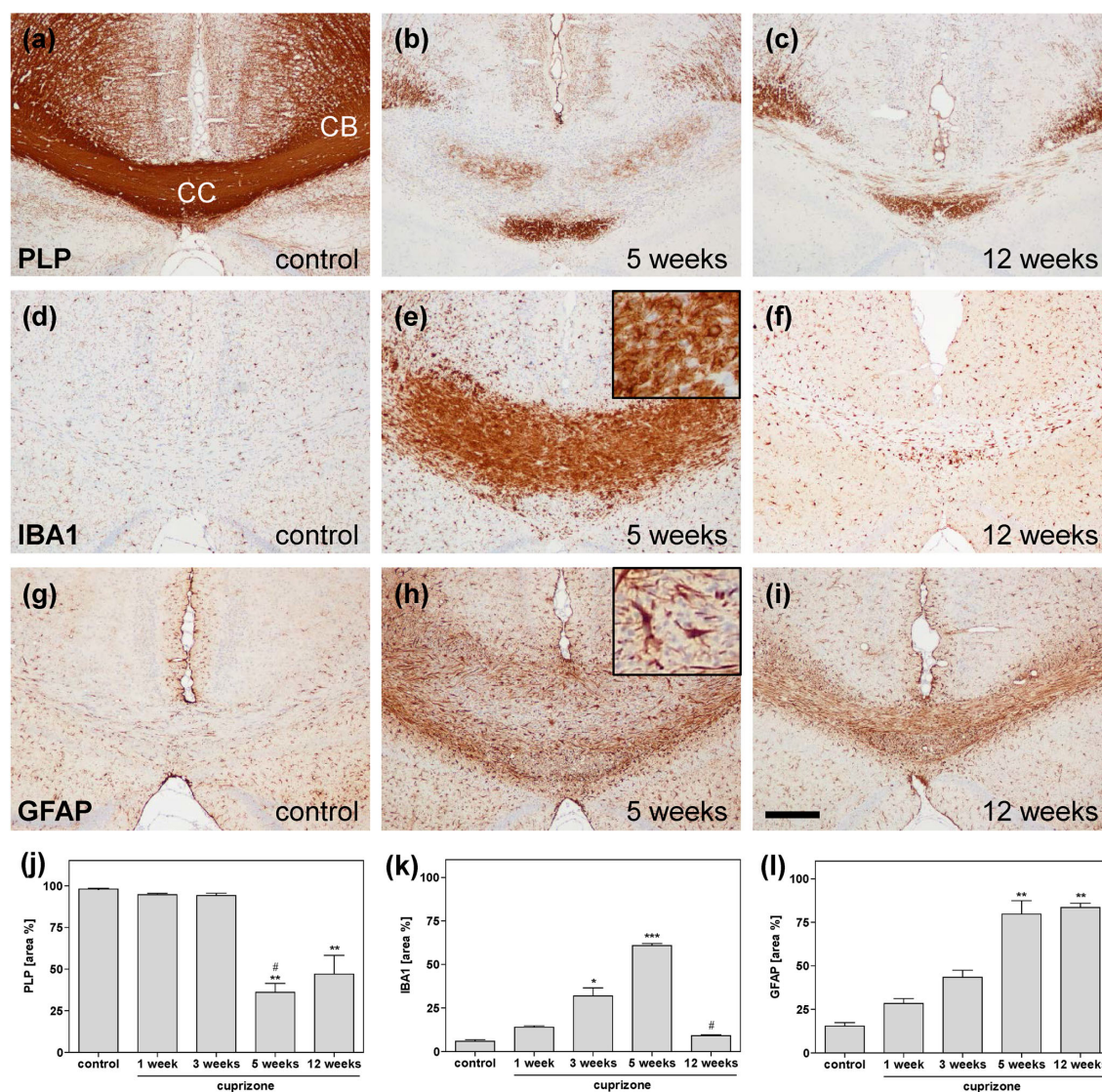


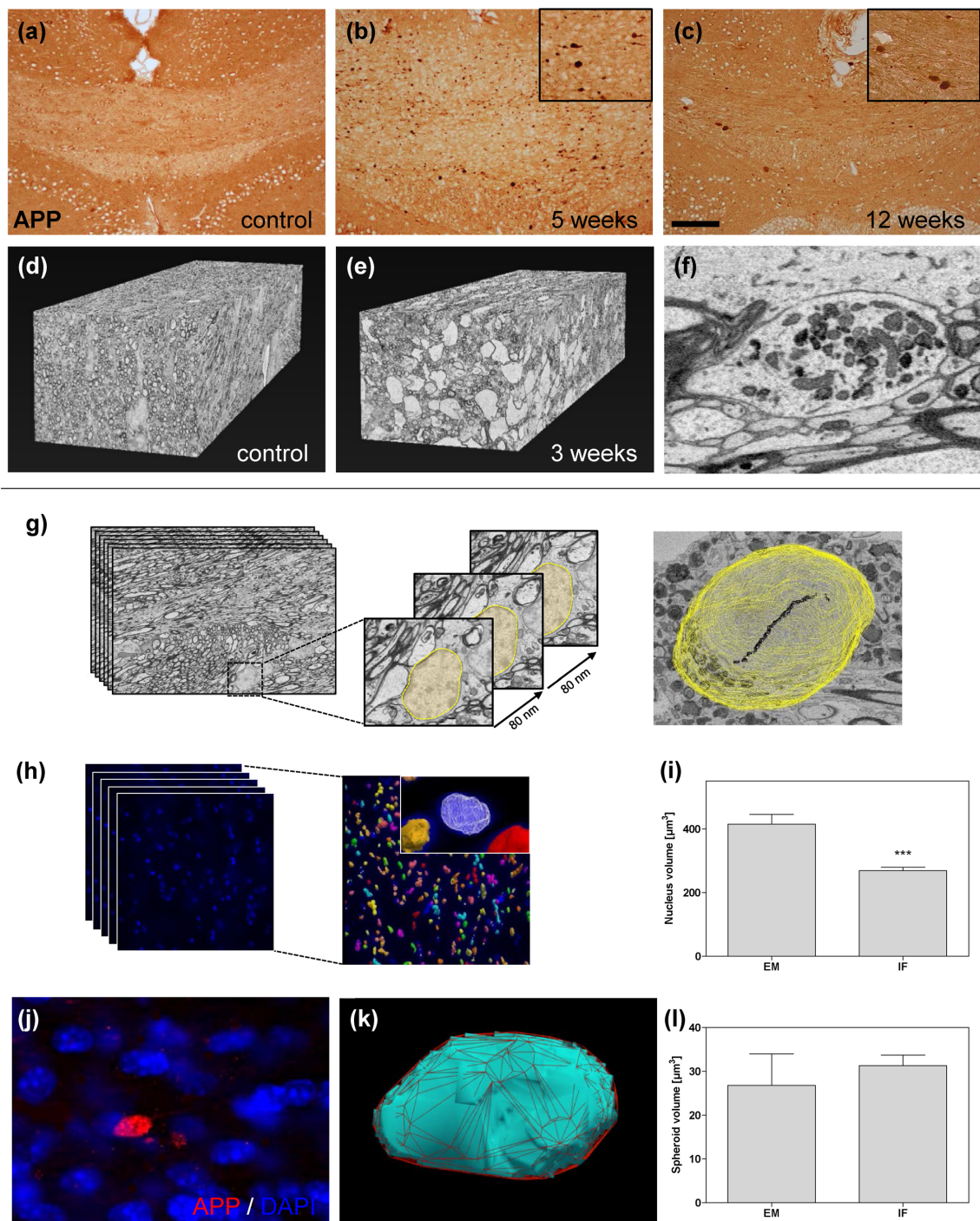
Fig. 1 Immunohistochemical analysis of myelin and glial activation during cuprizone intoxication. Representative sections illustrate immunohistochemical staining for PLP, IBA1, and GFAP in the midline of the corpus callosum (CC) including the cingulum bundle (CB) of controls (a, d, g) and after acute (b, e, h) and chronic demyelination (c,

f, i). Densitometric analysis of anti-PLP (j), anti-IBA1 (k), and anti-GFAP (l) stained sections. Four to five animals per group; one independent experiment. Significant differences are indicated by asterisks (vs controls) and hashtags (vs preceding time point) (* $p < 0.5$; ** $p < 0.01$; *** $p < 0.001$). Scale bar = 200 μm

present around neuronal cell bodies what appeared to be excitatory boutons. As one would expect, VGLUT1⁺ signals appeared as small granular spots (Fig. 3a), indicating specificity of the applied antibody. In the white matter (i.e., CC and CB) of control animals, VGLUT1 was virtually absent (Fig. 3a, d). During cuprizone-induced demyelination, the densities of VGLUT1⁺ spheroids gradually increased until week 5 (Fig. 3b, d). At week 12, the density of VGLUT1⁺ spheroids was slightly lower compared to week 5, the

diameter of individual VGLUT1⁺ spheroids was significantly larger (Fig. 3c–e).

The majority of axons in the CC are glutamatergic. However, there is rising evidence about inhibitory fibers, connecting the two hemispheres [35]. We next examined whether synaptic vesicles, synthesized by inhibitory neurons, as well accumulate in the demyelinated CC. The gray matter of control and cuprizone-treated animals displayed a fine granular VGAT⁺ staining, whereas the white matter of the



CC was virtually devoid of any VGAT⁺ signal (Fig. 3f). Of note, VGAT did not accumulate as spheroids during cuprizone-induced demyelination (Fig. 3g, h).

Since we observed accumulation of mitochondria in axonal swellings on the ultrastructural level, we next looked for the localization of mitochondrial proteins by immunohistochemistry.

Fig. 2 Immunohistochemical and ultrastructural analysis of axonal damage. Representative sections illustrate immunohistochemical staining for amyloid precursor protein (APP) in the midline of the corpus callosum in controls (a), after acute (b) and chronic (c) demyelination. Three-dimensional (3D) reconstructions of 3D electron microscopy (EM) images of the CC of control (d) and 3 weeks cuprizone-treated animals (e). The EM image shows a focal axonal swelling filled with mitochondria and synaptic vesicles in the CC of cuprizone-fed mice (f). Cell nuclei in EM images were reconstructed by tracing their outlines using ImageJ (g). Cell nuclei in APP-immunofluorescence (IF) images were reconstructed using NeuroLucida360 (h). Volume of cell nuclei in EM and APP-IF images (i). Representative image and reconstruction of an APP⁺ spheroid (j, k). Spheroid volume of 3D EM and APP-IF images after correction of tissue shrinkage or swelling artifacts (l). Four animals per group; one independent experiment. Statistically significant differences are indicated by asterisks (***## $p < 0.001$). Scale bar = 100 μm (a–c)

COX4 is located in the inner mitochondrial membrane, while VDAC1, also known as mitochondrial porin, is a channel of the outer mitochondrial membrane, respectively. Both were strongly expressed in the gray matter of control animals. VDAC1 and COX4 signals appeared as fine granular spots within the neuropil, along with a stronger cytoplasmic staining (Fig. 4a, d). In contrast, the white matter was virtually devoid of VDAC1⁺ and COX4⁺ signals (Fig. 4a, d), at least at the applied antibody concentrations. During demyelination, VDAC1⁺ and COX4⁺ spheroids densities increased till week 5 (Fig. 4b, e, g, h). Such relatively big VDAC1⁺ and COX4⁺ spheroids were not in a spatial relation to cell nuclei. Of note, at week 5, we observed as well high densities of small COX4⁺ and VDAC1⁺ dots, which were frequently found in close proximity to a nucleus. These

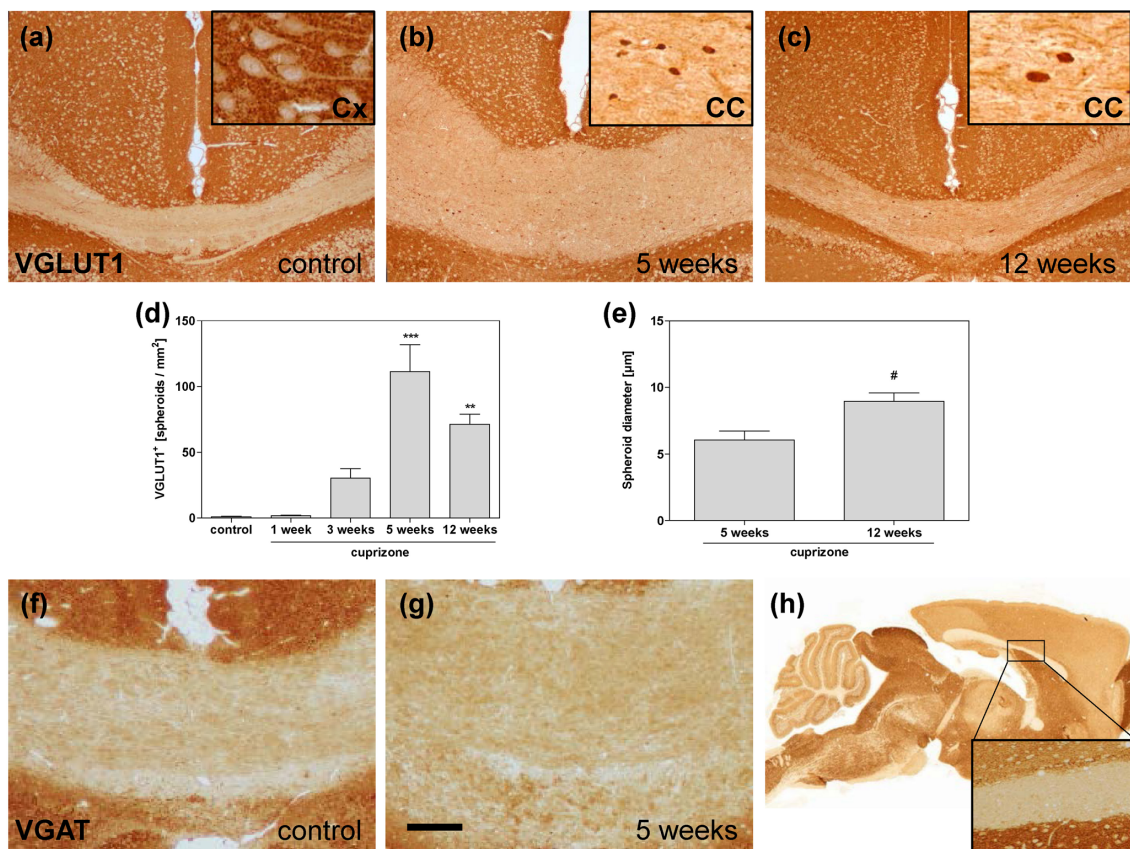


Fig. 3 Immunohistochemical analysis of vesicular proteins. Representative sections illustrate immunohistochemical staining for VGLUT1 in the cortex (Cx) and corpus callosum (CC) of control animals (a), after acute (b) and chronic demyelination (c). Insets show higher magnification of VGLUT1 in the Cx and the CC. Quantification of VGLUT1⁺ spheroids during cuprizone-induced demyelination (d). Spheroid diameter after acute and chronic demyelination (e).

Representative images show VGAT immunohistochemistry in controls (f) and coronal and sagittal sections of cuprizone-intoxicated mice (g, h). Five to seven animals per group; two independent experiments. Statistically significant differences are indicated by asterisks (vs controls) and hashtags (vs preceding time point) (*# $p < 0.5$; ***## $p < 0.001$). Scale bar = 200 μm (a–c); 100 μm (f, g)

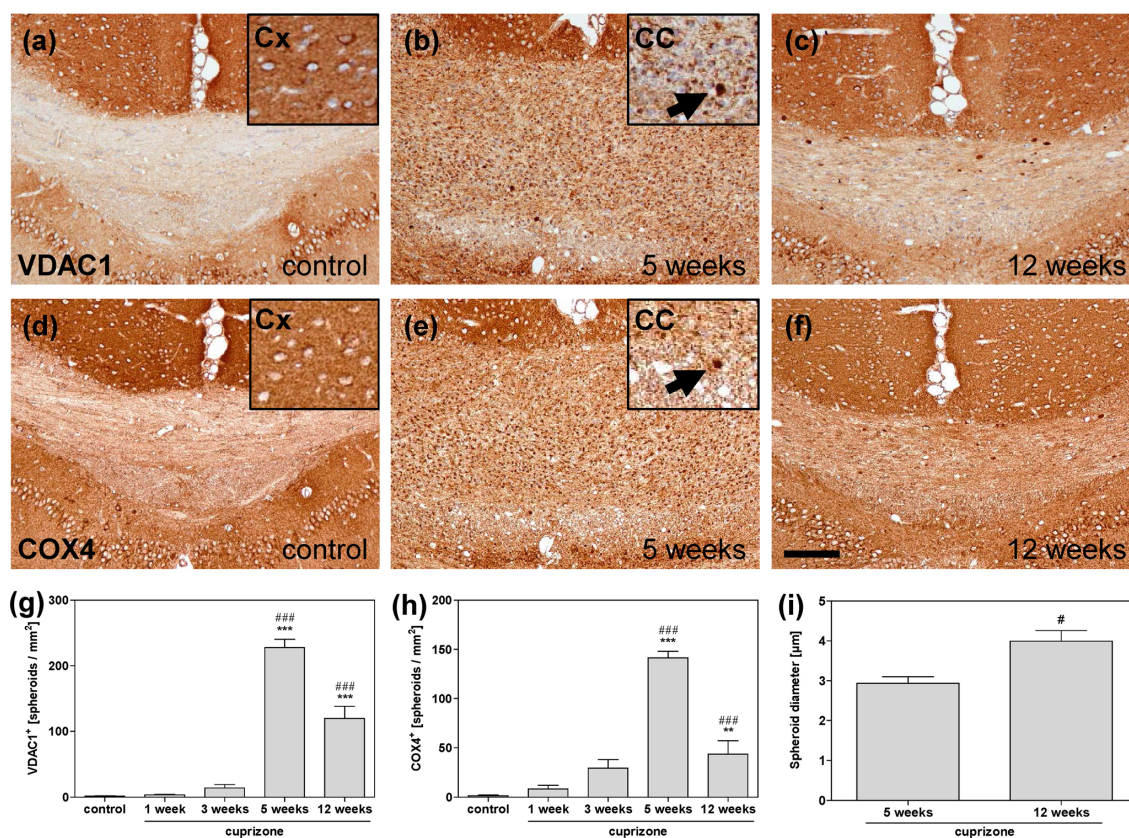


Fig. 4 Immunohistochemical analysis of mitochondrial proteins. Representative sections illustrate immunohistochemical staining for VDAC1 and COX4 in the corpus callosum (CC) of controls (a, d) and during acute (b, e) and chronic demyelination (c, f). Insets show higher magnification of VDAC1 and COX4 in the cortex (Cx) and CC. Quantification of VDAC1⁺ (g) and COX4⁺ (h) spheroids after

cuprizone-induced demyelination. COX4⁺ spheroids increased in size during cuprizone-induced demyelination (i). Five to nine animals per group; two independent experiments. Statistically significant differences are indicated by asterisks (vs controls) and hashtags (vs preceding time point) (*# $p < 0.5$; **## $p < 0.01$; ***### $p < 0.001$). Scale bar = 100 μm

small dots probably represent mitochondria in activated microglia and/or astrocytes. At week 12, densities of VDAC1⁺ and COX4⁺ spheroids were decreased, while the spheroid size was increased compared to week 5 (Fig. 4c, f–i). Beyond, the fine-grained, perinuclear staining pattern was robustly reduced at week 12, further indicating that this fine staining pattern reflects microglial mitochondria rather than mitochondria within axonal spheroids.

Vesicular and Mitochondrial Spheroids Serve as Marker for Axonal Damage

To verify VGLUT1 as a marker for axonal injury, we performed co-localization studies for VGLUT1 and APP. VGLUT1/APP double staining revealed co-localization of

VGLUT1⁺ and APP⁺ spheroids after acute and chronic demyelination (Fig. 5a–f). Around one quarter of spheroids were VGLUT1⁺/APP⁺ after 5 weeks of cuprizone treatment, shifting to one third of spheroids at the 12-week time point. VGLUT1[−]/APP⁺ spheroids comprised the majority of spheroids at both time points, ranging from 64% (acute demyelination) to 49% (chronic demyelination), whereas just some axonal spheroids were VGLUT1 single positive (Fig. 5g).

It has been suggested that VGLUT1 is expressed in synaptic-like microvesicles of astrocytes [23, 36, 37]. We were, thus, next interested whether VGLUT1 single positive spheroids belong to the astrocyte population. To investigate this, we first performed immunofluorescence double staining experiments with anti-VGLUT1 and anti-GFAP antibodies. As shown, VGLUT1 did not co-localize with GFAP⁺ astro-

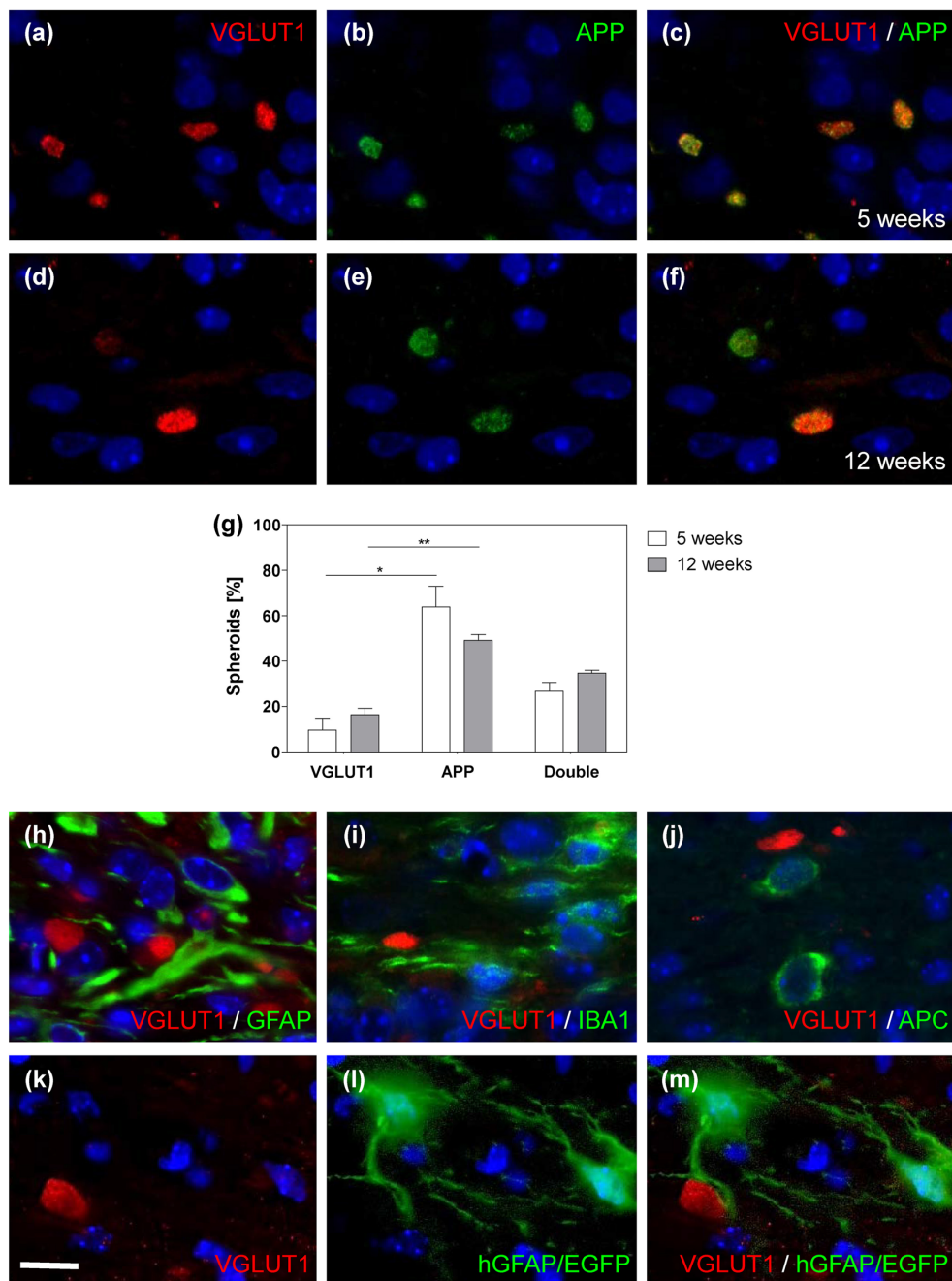


Fig. 5 VGLUT as a marker for axonal damage. VGLUT1 and APP colocalize in the corpus callosum during acute (a–c) and chronic demyelination (d–f). Quantification of APP⁺, VGLUT1⁺, and APP⁺/VGLUT1⁺ spheroids (g). VGLUT1 does not co-localize with the astrocytic marker GFAP (h), the microglial marker IBA1 (i), or the

oligodendroglial marker APC (j). VGLUT1 also does not co-localize with hGFAP EGFP⁺ astrocytes (k–m). Three to five animals per group; one independent experiment. Statistically significant differences are indicated by asterisks (** $p < 0.01$; * $p < 0.05$). Scale bar = 10 μ m

cytes in the CC (Fig. 5h). To further confirm this result, we performed anti-VGLUT1 immunofluorescence staining in hGFAP-EGFP-mice. These mice express GFAP not only in proximal processes, but also in fine distal processes of astrocytes [30]. In line with our results obtained by fluorescence-double labeling, we did not find any co-localization of VGLUT1 and GFAP in the CC (Fig. 5k–m). Furthermore, VGLUT1 did neither co-localize with IBA1⁺ microglia nor APC⁺ mature oligodendrocytes in the CC (Fig. 5i, j). In summary, this series of experiments suggests that VGLUT1 accumulates in injured axons.

Next, we investigated whether co-localization of vesicles and mitochondria, as evident on the ultrastructural level, could also be observed by immunohistochemistry. Co-localization of APP and COX4 was found in the CC after acute and chronic demyelination (Fig. 6a–f). Comparable to our results obtained by VGLUT1/APP double labeling, COX4⁻/APP⁺ spheroids were more numerous than COX4⁺/APP⁺ spheroids (Fig. 6g). Mitochondria are found in the cytoplasm of almost all eukaryotic cells. In order to confirm that COX4 single positive spheroids represent axonal accumulations, immunofluorescence double stains for COX4 and glia cell markers were performed. COX4⁺ spheroids did neither co-localize with GFAP⁺ astrocytes, IBA1⁺ microglia, nor APC⁺ mature oligodendrocytes (Fig. 6h–j). However, perinuclear COX4 signal was detected in IBA1 positive microglia in the CC of cuprizone-treated animals (Fig. 6i). This suggests that small COX4⁺ spots represent mitochondria of glial cells, while structures without nuclear staining represent axonal accumulations.

Finally, we compared the sensitivity of APP, VGLUT1, VDAC1, and COX4 as markers for axonal injury during acute and chronic demyelination. In acute lesions, numbers of VGLUT1⁺, VDAC1⁺, and COX4⁺ spheroids were significantly lower compared to APP⁺ spheroids (Fig. 7a; Table 1). After chronic demyelination, numbers of spheroids were similar for VGLUT1 and COX4, while numbers of VDAC1⁺ spheroids tended to be higher (Fig. 7b). These data indicate that APP is, among the analyzed proteins, the most sensitive marker for axonal transport disturbances after acute demyelination, while this is not the case after chronic demyelination.

Vesicular and Mitochondrial Proteins Accumulate as Spheroids in MS Lesions

Chronic active lesions were demyelinated and hypocellular with accumulations of macrophages/microglia at the lesion border (Fig. 8a, b). To analyze whether acute axonal damage is present in chronic active MS lesions, consecutive sections were stained for APP. In affected white matter areas, numerous APP⁺ spheroids were found in the center and border of the lesion (Fig. 8c). To verify whether lesions as well contain

VGLUT1⁺ and COX4⁺ spheroids, we next performed immunohistochemistry for VGLUT1 and COX4. Both, VGLUT1⁺ and COX4⁺ spheroids were found in the affected white matter (Fig. 8d, e), while the normal appearing white matter was virtually devoid of spheroids positive for VGLUT1 and COX4. As expected, perinuclear COX4⁺ staining was regularly seen in lesions and non-lesion areas. Additionally, VGLUT1⁺ glial-like structures could be observed in lesions and the surrounding tissue (not shown). To confirm that VGLUT1⁺ spheroids resemble axonal damage in human MS lesions, we performed co-localization studies of VGLUT1 and APP. The vast majority of spheroids were positive for APP, while just a minor number of spheroids was VGLUT1⁺/APP⁺ (Fig. 8f–h).

Discussion

Organelle and vesicle transport is vital for the maintenance of axonal health, in which the distances between sites of organelle biogenesis, function, and recycling or degradation can be vast. To better understand the signature of axonal transport deficits and damage, we selectively investigated vesicular and mitochondrial transport deficits, and compared ultrastructural and histological morphologies.

We first determined the level of axonal damage in the cuprizone model using anti-APP immunohistochemistry, which is a standard method for detecting axonal transport deficits and, hence, acute axonal injury [4, 13, 14, 38]. In line with previous results, we observed accumulation of APP after acute and chronic cuprizone-induced demyelination [15, 20]. Accumulations of APP have also been observed in other MS animal models including experimental autoimmune encephalomyelitis (EAE) and the lysophosphatidylcholine-induced demyelination model [15, 39]. Findings from EAE experiments suggest that alterations in axonal transport is an early event and not simply the consequence of disease progression [40].

To determine whether APP⁺ spheroids represent axonal swellings observed on the ultrastructural level, we first compared the volumes of axonal spheroids/swellings using two different methods (i.e., confocal anti-APP immunofluorescence stains and 3D EM). For most studies exploring axonal damage, either one or the other method was used [14, 27]. To the best of our knowledge, this is the first study comparing both methods site by site. Therefore, tissue of 3 weeks cuprizone intoxication was used since intoxication with cuprizone for 5 weeks results in severe demyelination and tissue damage. After 3 weeks, the CC is only partly demyelinated, the morphology is largely preserved, and axonal swellings can be clearly identified. During tissue embedding, the true volumes of cells and cellular processes can change because of tissue shrinkage or swelling, respectively.

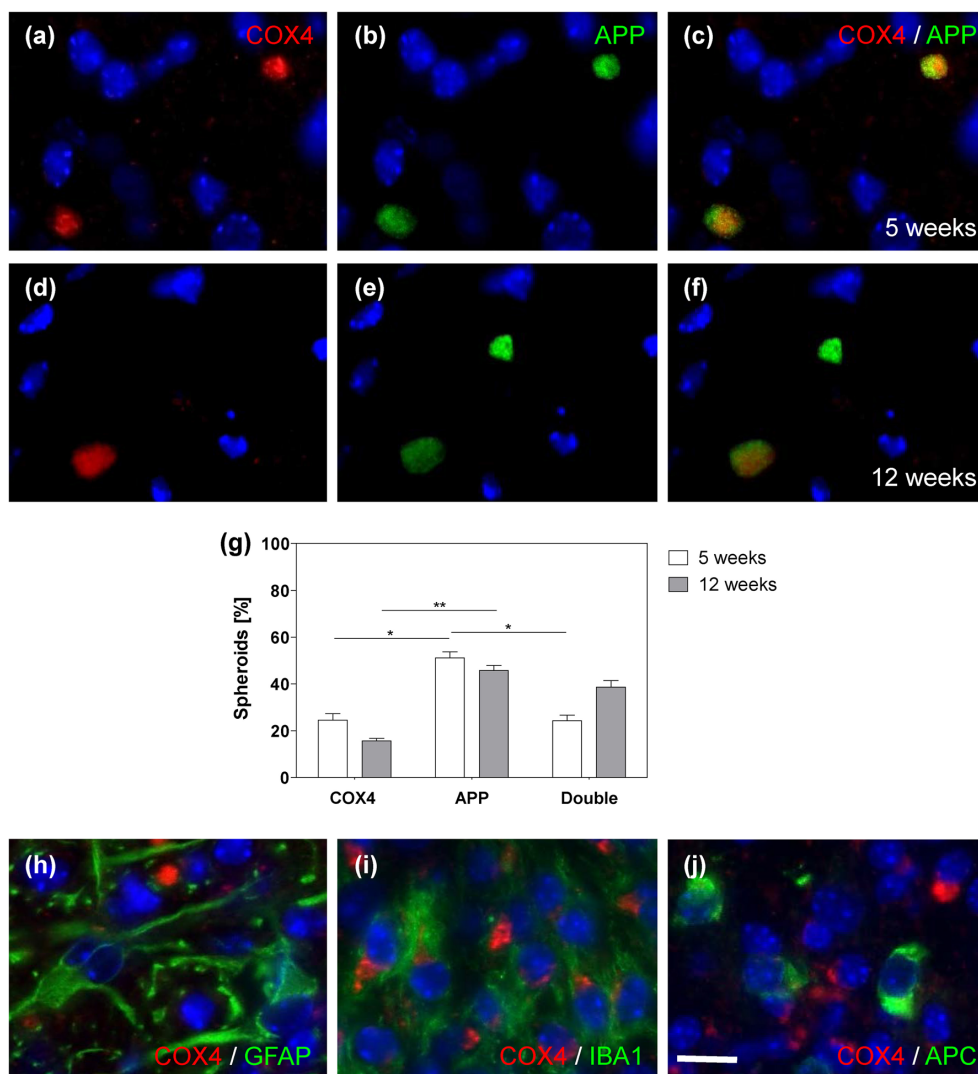


Fig. 6 COX4 as a marker for axonal damage. COX4 and APP co-localize in the corpus callosum during acute (a–c) and chronic demyelination (d–f). Quantification of APP⁺, COX4⁺, and APP⁺/COX4⁺spheroids (g). COX4⁺ spheroids do not co-localize with the astrocytic marker GFAP (h), microglial marker IBA1 (i), or the oligodendroglial marker APC (j).

Perinuclear COX4 co-localizes with the microglial marker IBA1 (i). Five animals per group; one independent experiment. Statistically significant differences are indicated by asterisks (* $p < 0.05$, ** $p < 0.01$). Scale bar = 10 μ m

To account for different extends of shrinkage or swelling artifacts in our differentially processed tissues (i.e., immunofluorescence versus 3D EM), we first measured the volume of cell nuclei in both approaches and thereby determined a “normalization value.” Then, we quantified volumes of anti-APP⁺ spheroids in free-floating sections and compared them to volumes of axonal swellings quantified in 3D EM images. As demonstrated in our studies, the mean spheroids volumes were not different from mean axonal swelling volumes if we accounted for tissue artifacts.

3D EM can be considered as gold standard method to detect axonal damage in our days. Using this method, whole axons can be tracked and reconstructed and any anomaly including axonal swellings can be made visible [27]. Furthermore, densely packed vesicles and mitochondria can be demonstrated in axonal swellings. In line with this, Ohno and colleagues showed in EM images axonal swellings filled with densely packed membranous organelles, including mitochondria [27]. Thus, the identification and localization of ultrastructural changes using 3D EM

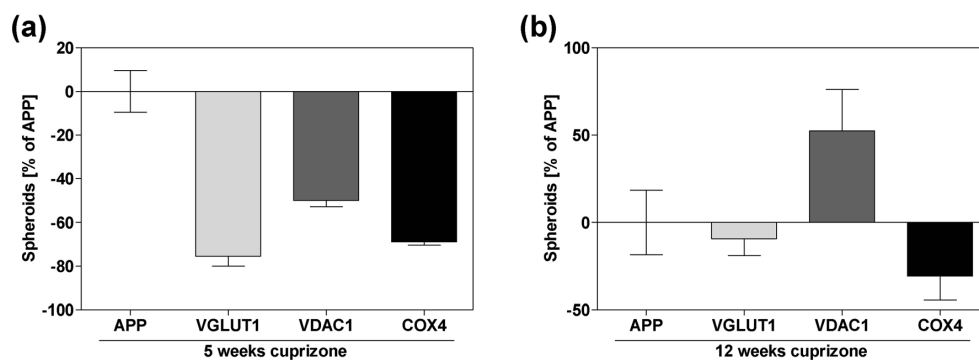


Fig. 7 Graphs show the ratio of VGLUT1⁺, VDAC1⁺ or COX4⁺ spheroids in relation to APP⁺ spheroids during acute (a) and chronic (b) demyelination

provides valuable information. However, EM images provide no information about individual vesicles and their contents. Immunohistochemistry is needed to characterize the accumulated vesicles and organelles on the biochemical level. Thus, the combination of immunohistochemistry and 3D EM provides a powerful tool to study the extent and signature of acute axonal injury. By means of immunohistochemistry, we could show that different vesicular (APP and VGLUT1) as well as mitochondrial (VDAC1 and COX4) proteins accumulate as axonal spheroids. In line with accumulation of APP⁺ spheroids, densities of vesicular and mitochondrial spheroids was most intense in areas of intense microgliosis. Previous studies report organelle accumulations before obvious demyelination [7, 40]. This indicates a complex pathomechanism, which is not simply a direct consequence of demyelination. Data from previous studies suggest a strong correlation between microglia/macrophages activation and axonal transport deficits [7], which we could also observe in our study.

Interestingly, we observed high densities of small vesicular and mitochondrial spheroids during acute demyelination, while we found less, but larger spheroids during chronic demyelination. Increased spheroid diameters are likely caused by the accumulation of more cargos at the side of permanent axonal damage. Another explanation would be that smaller axons are affected during acute demyelination, while larger axons may be involved during the chronic phase. Using *in vivo* imaging, it has been shown that axonal transport deficits are reversible [41]. At the beginning, spheroids appear to be a temporary

event, not caused by destruction of the microtubules and its components. It might be possible that cargos transiently “lose” their connection to binding proteins and microtubules under acute injury conditions and later find back to their destination. Thus, it was proposed by Gudi and colleagues that large spheroids represent permanent axonal damage, while smaller spheroids might represent reversible transport deficits [7]. It would now be interesting to systematically analyze the molecular composition of large versus small axonal spheroids by, for example, immunogold labeling experiments or, as performed in this study, immunofluorescence.

Another important observation in this study is the absence of VGAT⁺ spheroids in the demyelinated CC. It has been suggested that GABAergic as well as glutamatergic neurons send their axons through the CC [35]. We were initially surprised that damaged axons were not labeled with VGAT. The fact that VGAT immunoreactivity is found only in terminal regions in the cortex and not in damaged axons may mean that (i) axons of inhibitory neurons or the specific transport mechanism of VGAT⁺ vesicles are not affected or that (ii) relatively small numbers of vesicles filled with VGAT are transported along the axons. Thus, the small amount of accumulated VGAT might be beneath the immunohistochemical detection limit. The latter seems more likely, since loss and damage of GABAergic interneurons have been previously shown [42–44]. In this study, we further showed not only vesicular but also mitochondrial accumulations. Mitochondria play a pivotal role in homeostasis and function of neurons

Table 1 Details of the statistical analysis of spheroid counts during active (5 weeks) and chronic demyelination (12 weeks). *** $p < 0.001$

	5 weeks (mean ± SEM)	<i>p</i> (vs APP)	12 weeks (mean ± SEM)	<i>p</i> (vs APP)	% of 5 weeks
APP/mm ²	454.3 ± 43.4	–	78.4 ± 14.5	–	17.3
VGLUT1/mm ²	111.3 ± 20.5	***	71.2 ± 7.6	ns	64.0
VDAC1/mm ²	227.7 ± 12.5	***	119.6 ± 18.7	ns	52.5
COX4/mm ²	141.4 ± 6.7	***	54.3 ± 10.8	ns	38.4

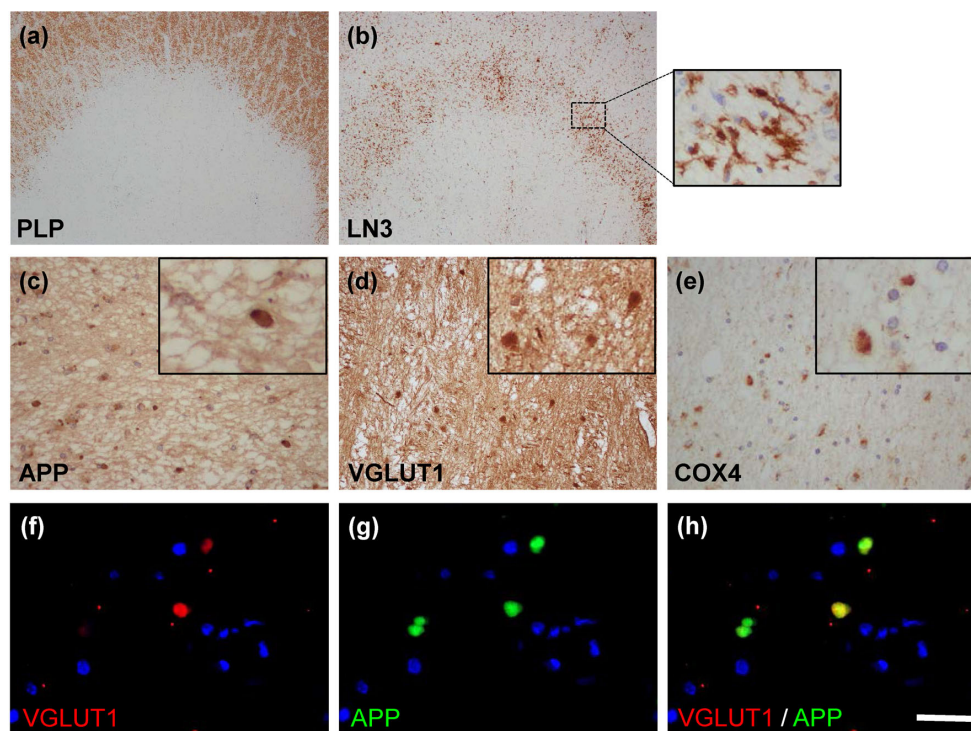


Fig. 8 Representative images show the extent of demyelination (PLP) (a) and inflammation (LN3, MHC-II to visualize antigen-presenting cells) (b) in a chronic active MS lesion. Representative images for APP⁺ (c),

VGLUT1⁺ (d), and COX4⁺ (e) spheroids in chronic active MS lesions. Co-localization of APP and VGLUT1 (f–h). Scale bar = 580 μ m (a, b); 10 μ m (e–e); 25 μ m (f–h)

and increasing evidence suggests that dysfunction of axonal mitochondria and mitochondrial transport are implicated in degeneration of axons [45, 46]. Disturbed transport and accumulation of mitochondria may cause local energy depletion and changes in calcium buffering. Furthermore, dysfunctional mitochondria may release reactive oxygen species that lead to increased axon vulnerability [47]. Studies in EAE mice have described axonal accumulation of COX4⁺ mitochondria in correlation with axonal degeneration [48]. Additionally, swellings of axons and mitochondrial pathology was observed at the side of focal axonal degeneration in EAE and active MS lesions [41]. In the present study, we could also identify COX4⁺ accumulations at side of axonal damage. Mitochondria are not only important for proper neuronal functioning, but also for glial cells [49]. Here, we found that small COX4⁺ dots appear in high numbers in activated microglia during acute demyelination. Thus, COX4 may serve not only as a marker for axonal damage, when accumulated as spheroids, but might also represent glial activation. Of note, careful examination of the tissues allow, based on nuclear co-localization, a distinction between mitochondria accumulating in glia cells versus mitochondria accumulating in axonal spheroids.

In summary, the current results demonstrate a vesicular as well as mitochondrial accumulation at sites of acute axonal injury, not only in the cuprizone model, but also in MS lesions. We propose that the combination of 3D EM and immunohistochemistry serves as a valuable tool to study axonal damage in more detail and that specific proteins, including VGLUT1 and COX4, could serve as selective markers for axonal damage. Further studies, especially in autopsy material, are required to ascertain how vesicular and mitochondrial accumulations vary in different types of lesions and different clinical phenotypes. A better understanding of axonal injury might thus contribute to the development of potential treatments which ameliorate or even reverse axonal pathology in MS.

Acknowledgments We thank Christiane Nolte and Helmut Kettenmann for providing hGFAP/EGFP transgenic mice (Max-Delbrueck Center for Molecular Medicine in the Helmholtz Association, Berlin, Germany). We thank Sarah Wübbel, Astrid Baltruschat, and Beate Aschauer for their excellent and valuable technical assistance.

Compliance with Ethical Standards

Conflict of Interest The authors declare that they have no conflict of interest.

References

- Lublin FD, Reingold SC (1996) Defining the clinical course of multiple sclerosis: results of an international survey. National Multiple Sclerosis Society (USA) Advisory Committee on Clinical Trials of New Agents in Multiple Sclerosis. *Neurology* 46(4):907–911
- Kipp M, Nyamoya S, Hochstrasser T, Amor S (2017) Multiple sclerosis animal models: a clinical and histopathological perspective. *Brain Pathol (Zurich, Switzerland)* 27(2):123–137. <https://doi.org/10.1111/bpa.12454>
- Hochstrasser T, Jiangshan Z, Ruhling S, Schmitz C, Kipp M (2018) Do pre-clinical multiple sclerosis models allow us to measure neurodegeneration and clinical progression? *Expert Rev Neurother* 18:1–3. <https://doi.org/10.1080/14737175.2018.1459190>
- Kuhlmann T, Lingfeld G, Bitsch A, Schuchardt J, Bruck W (2002) Acute axonal damage in multiple sclerosis is most extensive in early disease stages and decreases over time. *Brain J Neurol* 125(Pt 10):2202–2212
- Schirmer L, Antel JP, Bruck W, Stadelmann C (2011) Axonal loss and neurofilament phosphorylation changes accompany lesion development and clinical progression in multiple sclerosis. *Brain Pathol (Zurich, Switzerland)* 21(4):428–440. <https://doi.org/10.1111/j.1750-3639.2010.00466.x>
- Trapp BD, Peterson J, Ransohoff RM, Rudick R, Mork S, Bo L (1998) Axonal transection in the lesions of multiple sclerosis. *N Engl J Med* 338(5):278–285. <https://doi.org/10.1056/nejm199801293380502>
- Gudi V, Gai L, Herder V, Tejedor LS, Kipp M, Amor S, Suhs KW, Hansmann F et al (2017) Synaptophysin is a reliable marker for axonal damage. *J Neuropathol Exp Neurol* 76:109–125. <https://doi.org/10.1093/jnen/nlw114>
- Koo EH, Sisodia SS, Archer DR, Martin LJ, Weidemann A, Beyreuther K, Fischer P, Masters CL et al (1990) Precursor of amyloid protein in Alzheimer disease undergoes fast anterograde axonal transport. *Proc Natl Acad Sci U S A* 87(4):1561–1565
- Groemer TW, Thiel CS, Holt M, Riedel D, Hua Y, Huve J, Wilhelm BG, Klingauf J (2011) Amyloid precursor protein is trafficked and secreted via synaptic vesicles. *PLoS One* 6(4):e18754. <https://doi.org/10.1371/journal.pone.0018754>
- Tyan SH, Shih AY, Walsh JJ, Maruyama H, Sarsoza F, Ku L, Eggert S, Hof PR et al (2012) Amyloid precursor protein (APP) regulates synaptic structure and function. *Mol Cell Neurosci* 51(1–2):43–52. <https://doi.org/10.1016/j.mcn.2012.07.009>
- Sheriff FE, Bridges LR, Gentleman SM, Sivaloganathan S, Wilson S (1994) Markers of axonal injury in post mortem human brain. *Acta Neuropathol* 88(5):433–439
- Stone JR, Singleton RH, Povlishock JT (2000) Antibodies to the C-terminus of the beta-amyloid precursor protein (APP): a site specific marker for the detection of traumatic axonal injury. *Brain Res* 871(2):288–302
- Ferguson B, Matyszak MK, Esiri MM, Perry VH (1997) Axonal damage in acute multiple sclerosis lesions. *Brain J Neurol* 120(Pt 3):393–399
- Bitsch A, Schuchardt J, Bunkowski S, Kuhlmann T, Bruck W (2000) Acute axonal injury in multiple sclerosis. Correlation with demyelination and inflammation. *Brain J Neurol* 123(Pt 6):1174–1183
- Hoflich KM, Beyer C, Clarner T, Schmitz C, Nyamoya S, Kipp M, Hochstrasser T (2016) Acute axonal damage in three different murine models of multiple sclerosis: a comparative approach. *Brain Res* 1650:125–133. <https://doi.org/10.1016/j.brainres.2016.08.048>
- Buschmann JP, Berger K, Awad H, Clarner T, Beyer C, Kipp M (2012) Inflammatory response and chemokine expression in the white matter corpus callosum and gray matter cortex region during cuprizone-induced demyelination. *Journal of molecular neuroscience : MN* 48(1):66–76. <https://doi.org/10.1007/s12031-012-9773-x>
- Kipp M, Clarner T, Dang J, Copray S, Beyer C (2009) The cuprizone animal model: new insights into an old story. *Acta Neuropathol* 118(6):723–736. <https://doi.org/10.1007/s00401-009-0591-3>
- Vana AC, Flint NC, Harwood NE, Le TQ, Fruttiger M, Armstrong RC (2007) Platelet-derived growth factor promotes repair of chronically demyelinated white matter. *J Neuropathol Exp Neurol* 66(11):975–988. <https://doi.org/10.1097/NEN.0b013e3181587d46>
- Mason JL, Langaman C, Morell P, Suzuki K, Matsushima GK (2001) Episodic demyelination and subsequent remyelination within the murine central nervous system: changes in axonal calibre. *Neuropathol Appl Neurobiol* 27(1):50–58
- Lindner M, Fokuhl J, Linsmeier F, Trebst C, Stangel M (2009) Chronic toxic demyelination in the central nervous system leads to axonal damage despite remyelination. *Neurosci Lett* 453(2):120–125. <https://doi.org/10.1016/j.neulet.2009.02.004>
- Hennequin G, Agnes EJ, Vogels TP (2017) Inhibitory plasticity: balance, control, and codependence. *Annu Rev Neurosci* 40:557–579. <https://doi.org/10.1146/annurev-neuro-072116-031005>
- Sheng M, Kim MJ (2002) Postsynaptic signaling and plasticity mechanisms. *Science (New York, NY)* 298(5594):776–780. <https://doi.org/10.1126/science.1075333>
- Freneau RT Jr, Voglmaier S, Seal RP, Edwards RH (2004) VGLUTs define subsets of excitatory neurons and suggest novel roles for glutamate. *Trends Neurosci* 27(2):98–103. <https://doi.org/10.1016/j.tins.2003.11.005>
- McIntire SL, Reimer RJ, Schuske K, Edwards RH, Jorgensen EM (1997) Identification and characterization of the vesicular GABA transporter. *Nature* 389(6653):870–876. <https://doi.org/10.1038/39908>
- Liguz-Leczna M, Skangiel-Kramska J (2007) Vesicular glutamate transporters (VGLUTs): the three musketeers of glutamatergic system. *Acta Neurobiol Exp* 67(3):207–218
- Andrews H, White K, Thomson C, Edgar J, Bates D, Griffiths I, Turnbull D, Nichols P (2006) Increased axonal mitochondrial activity as an adaptation to myelin deficiency in the Shiverer mouse. *J Neurosci Res* 83(8):1533–1539. <https://doi.org/10.1002/jnr.20842>
- Ohno N, Chiang H, Mahad DJ, Kidd GJ, Liu L, Ransohoff RM, Sheng ZH, Komuro H et al (2014) Mitochondrial immobilization mediated by syntaphilin facilitates survival of demyelinated axons. *Proc Natl Acad Sci U S A* 111(27):9953–9958. <https://doi.org/10.1073/pnas.1401155111>
- Han SM, Baig HS, Hammarlund M (2016) Mitochondria localize to injured axons to support regeneration. *Neuron* 92(6):1308–1323. <https://doi.org/10.1016/j.neuron.2016.11.025>
- Karbowska M, Neutzner A (2012) Neurodegeneration as a consequence of failed mitochondrial maintenance. *Acta Neuropathol* 123(2):157–171. <https://doi.org/10.1007/s00401-011-0921-0>
- Nolte C, Matyash M, Pivneva T, Schipke CG, Ohlemeyer C, Hanisch UK, Kirchhoff F, Kettenmann H (2001) GFAP promoter-controlled EGFP-expressing transgenic mice: a tool to visualize astrocytes and astrogliosis in living brain tissue. *Glia* 33(1):72–86
- Seewann A, Kooi EJ, Roosendaal SD, Barkhof F, van der Valk P, Geurts JJ (2009) Translating pathology in multiple sclerosis: the combination of postmortem imaging, histopathology and clinical findings. *Acta Neurol Scand* 119(6):349–355. <https://doi.org/10.1111/j.1600-0404.2008.01137.x>
- Wagenknecht N, Becker B, Scheld M, Beyer C, Clarner T, Hochstrasser T, Kipp M (2016) Thalamus degeneration and inflammation in two distinct multiple sclerosis animal models. *J Mol Neurosci : MN* <https://doi.org/10.1007/s12031-016-0790-z>, 60, 102, 114

33. Hochstrasser T, Exner GL, Nyamoya S, Schmitz C, Kipp M (2017) Cuprizone-containing pellets are less potent to induce consistent demyelination in the corpus callosum of C57BL/6 mice. *Journal of molecular neuroscience* : MN 61(4):617–624. <https://doi.org/10.1007/s12031-017-0903-3>
34. Grosse-Veldmann R, Becker B, Amor S, van der Valk P, Beyer C, Kipp M (2015) Lesion expansion in experimental demyelination animal models and multiple sclerosis lesions. *Mol Neurobiol* 53: 4905–4917. <https://doi.org/10.1007/s12035-015-9420-y>
35. Rock C, Zurita H, Leiby S, Wilson CJ, Apicella AJ (2018) Cortical circuits of callosal GABAergic neurons. *Cerebral cortex (New York, NY : 1991)* 28(4):1154–1167. <https://doi.org/10.1093/cercor/bhx025>
36. Brumovsky PR (2013) VGLUTs in Peripheral Neurons and the Spinal Cord: Time for a Review. *ISRN Neurol*. <https://doi.org/10.1155/2013/829753>
37. Ormel L, Stensrud MJ, Bergersen LH, Gundersen V (2012) VGLUT1 is localized in astrocytic processes in several brain regions. *Glia* 60:229–238. <https://doi.org/10.1002/glia.21258>
38. Bramlett HM, Kraydieh S, Green EJ, Dietrich WD (1997) Temporal and regional patterns of axonal damage following traumatic brain injury: a beta-amyloid precursor protein immunocytochemical study in rats. *J Neuropathol Exp Neurol* 56(10):1132–1141
39. Herrero-Herranz E, Pardo LA, Gold R, Linker RA (2008) Pattern of axonal injury in murine myelin oligodendrocyte glycoprotein induced experimental autoimmune encephalomyelitis: implications for multiple sclerosis. *Neurobiol Dis* 30(2):162–173. <https://doi.org/10.1016/j.nbd.2008.01.001>
40. Sorbara CD, Wagner NE, Ladwig A, Nikic I, Merkler D, Kleele T, Marinkovic P, Naumann R et al (2014) Pervasive axonal transport deficits in multiple sclerosis models. *Neuron* 84(6):1183–1190. <https://doi.org/10.1016/j.neuron.2014.11.006>
41. Nikic I, Merkler D, Sorbara C, Brinkoetter M, Kreutzfeldt M, Bareyre FM, Bruck W, Bishop D et al (2011) A reversible form of axon damage in experimental autoimmune encephalomyelitis and multiple sclerosis. *Nat Med* 17(4):495–499. <https://doi.org/10.1038/nm.2324>
42. Lapato AS, Szu J, Hasselmann JP, Khalaj AJ, Binder DK, Tiwari-Woodruff SK (2017) Chronic demyelination-induced seizures. *Neuroscience* 346:409–422. <https://doi.org/10.1016/j.neuroscience.2017.01.035>
43. Rossi S, Muzio L, De Chiara V, Grasselli G, Musella A, Musumeci G, Mandolesi G, De Ceglia R et al (2011) Impaired striatal GABA transmission in experimental autoimmune encephalomyelitis. *Brain Behav Immun* 25(5):947–956. <https://doi.org/10.1016/j.bbi.2010.10.004>
44. Falco A, Pennucci R, Brambilla E, de Curtis I (2014) Reduction in parvalbumin-positive interneurons and inhibitory input in the cortex of mice with experimental autoimmune encephalomyelitis. *Exp Brain Res* 232(7):2439–2449. <https://doi.org/10.1007/s00221-014-3944-7>
45. Sheng ZH, Cai Q (2012) Mitochondrial transport in neurons: impact on synaptic homeostasis and neurodegeneration. *Nat Rev Neurosci* 13(2):77–93. <https://doi.org/10.1038/nrn3156>
46. Lin MT, Beal MF (2006) Mitochondrial dysfunction and oxidative stress in neurodegenerative diseases. *Nature* 443(7113):787–795. <https://doi.org/10.1038/nature05292>
47. Baltan S (2014) Excitotoxicity and mitochondrial dysfunction underlie age-dependent ischemic white matter injury. *Advances in neurobiology* 11:151–170. https://doi.org/10.1007/978-3-319-08894-5_8
48. Bando Y, Nomura T, Bochimoto H, Murakami K, Tanaka T, Watanabe T, Yoshida S (2015) Abnormal morphology of myelin and axon pathology in murine models of multiple sclerosis. *Neurochem Int* 81:16–27. <https://doi.org/10.1016/j.neuint.2015.01.002>
49. Rose J, Brian C, Woods J, Pappa A, Panayiotidis MI, Powers R, Franco R (2017) Mitochondrial dysfunction in glial cells: implications for neuronal homeostasis and survival. *Toxicology* 391:109–115. <https://doi.org/10.1016/j.tox.2017.06.011>

6. Paper II

Hochstrasser T, Rühling S, Hecher K, Fabisch KH, Chrzanowski U, Brendel M, Eckenweber F, Sacher C, Schmitz C, Kipp M. Stereological Investigation of Regional Brain Volumes after Acute and Chronic Cuprizone-Induced Demyelination. *Cells*. 2019 Sep 3;8(9):1024. doi: 10.3390/cells8091024. PMID: 31484353; PMCID: PMC6770802.



Article

Stereological Investigation of Regional Brain Volumes after Acute and Chronic Cuprizone-Induced Demyelination

Tanja Hochstrasser ^{1,2,*}, Sebastian Rühling ^{1,2}, Kerstin Hecher ^{1,2}, Kai H. Fabisch ^{1,2}, Uta Chrzanowski ^{1,2}, Matthias Brendel ³, Florian Eckenweber ³, Christian Sacher ³, Christoph Schmitz ¹ and Markus Kipp ^{2,*} 

¹ Department of Anatomy II, Ludwig-Maximilians-University of Munich, 80336 Munich, Germany

² Institute of Anatomy, Rostock University Medical Center, 18057 Rostock, Germany

³ Department of Nuclear Medicine, University Hospital, Ludwig-Maximilians-University of Munich, 81377 Munich, Germany

* Correspondence: tanja.hochstrasser@med.uni-muenchen.de (T.H.); markus.kipp@med.uni-rostock.de (M.K.); Tel.: +49-89-2180-72705 (T.H.); Fax: +49-89-2180-72683 (T.H.)

Received: 16 July 2019; Accepted: 30 August 2019; Published: 3 September 2019



Abstract: Brain volume measurement is one of the most frequently used biomarkers to establish neuroprotective effects during pre-clinical multiple sclerosis (MS) studies. Furthermore, whole-brain atrophy estimates in MS correlate more robustly with clinical disability than traditional, lesion-based metrics. However, the underlying mechanisms leading to brain atrophy are poorly understood, partly due to the lack of appropriate animal models to study this aspect of the disease. The purpose of this study was to assess brain volumes and neuro-axonal degeneration after acute and chronic cuprizone-induced demyelination. C57BL/6 male mice were intoxicated with cuprizone for up to 12 weeks. Brain volume, as well as total numbers and densities of neurons, were determined using design-based stereology. After five weeks of cuprizone intoxication, despite severe demyelination, brain volumes were not altered at this time point. After 12 weeks of cuprizone intoxication, a significant volume reduction was found in the corpus callosum and diverse subcortical areas, particularly the internal capsule and the thalamus. Thalamic volume loss was accompanied by glucose hypermetabolism, analyzed by [¹⁸F]-fluoro-2-deoxy-D-glucose (18F-FDG) positron-emission tomography. This study demonstrates region-specific brain atrophy of different subcortical brain regions after chronic cuprizone-induced demyelination. The chronic cuprizone demyelination model in male mice is, thus, a useful tool to study the underlying mechanisms of subcortical brain atrophy and to investigate the effectiveness of therapeutic interventions.

Keywords: multiple sclerosis; cuprizone; atrophy; design-based stereology; 18F-FDG

1. Introduction

Multiple sclerosis (MS) is a chronic, inflammatory demyelinating disease of the central nervous system. The majority of MS patients experience two clinical phases reflecting distinct but inter-related pathologies. The first phase is characterized by recurrent episodes of immune-driven inflammation and demyelination, from which the patients can recover completely (relapsing–remitting (RR) MS). In the second phase, a continuous progression of clinical, permanent disability can be observed, while the relapse frequency decreases [1,2]. This secondary disease phase is called secondary progressive MS (SPMS), and the findings of several imaging and pathological studies suggest that neuro-axonal damage plays a central role for the observed clinical disease progression [3–5]. Current therapeutic strategies for MS are beneficial during RRMS by modulating or suppressing immune function [6].

However, such therapies have no or just a moderate impact on the progressive phase, and therapeutic options effective in SPMS are still unsatisfactory [7].

Much of the research in MS focused on the inflammatory aspects of the disease. As a consequence, the inflammatory component of MS animal models, such as peripheral immune cell recruitment or T-cell-mediated oligodendrocyte pathology, was studied in detail [8–10]. In contrast, the neurodegenerative aspect of the disease is by far less frequently addressed and, if so, these studies merely focused on axonal degeneration [11,12]. In particular, brain atrophy, which is a key outcome measure during clinical studies [5,13,14], is almost never evaluated in MS animal models, although magnetic resonance imaging (MRI)-based protocols were published [15,16]. In MS patients, MRI measurements revealed white-matter lesions, as well as gray-matter atrophy of specific brain areas including cortical and subcortical gray matter [17–19]. The extent of atrophy was found to be more severe in the subcortex compared to the superficial cortex, and was found to correlate with cognitive performance and clinical disability in MS patients [19,20]. Thus, establishing the histological correlate of volumetric changes in the brain is of significant importance [21,22].

The cuprizone model is a well-established mouse model of MS. Following oral administration of the copper-chelating agent cuprizone, the mouse brain exhibits a variety of pathological alterations including demyelination of the white and gray matter, gliosis, and axonal damage [23,24]. While acute demyelination is usually induced by five weeks of cuprizone feeding, sustained (chronic) demyelination can be achieved by feeding mice with cuprizone for 12 weeks. Although axonal damage is found after acute and chronic demyelination in this model [11,12,25], there is little data available on neuronal loss and volumetric changes in the different vulnerable brain regions. Previous imaging studies revealed volumetric changes in the corpus callosum and the cortex after cuprizone intoxication [26–28]. Furthermore, histopathological studies showed neuronal pathologies, including loss of neurons in the hilus of the dentate gyrus, as well as loss of parvalbumin inhibitory interneurons in the hippocampus CA1 subregion of chronically demyelinated mice [29,30]. However, the extent of cortical and subcortical atrophy determined by standardized histological techniques (i.e., design-based stereology [31]) is still unexplored; therefore, the significance of this model to study the underlying mechanisms of brain atrophy in MS is unknown.

Thus, in the present study, we used design-based stereology to analyze callosal, cortical, and subcortical volumes, as well as neuron numbers and densities after acute and chronic cuprizone-induced demyelination.

2. Materials and Methods

2.1. Animals

Male C57BL/6J mice were purchased from Janvier (Le Genest-Saint-Isle, France), and were housed in a temperature-controlled environment (21–24 °C) with humidity levels between 55% and 65% on a 12-h light/dark cycle. Chow and water were provided ad libitum. All experiments were performed according to the Federation of European Laboratory Animal Science Association recommendations and were approved by the Review Board for the Care of Animal Subjects of the district government of Upper Bavaria (55.2-1-54-2532-73-15).

2.2. Cuprizone Intoxication and Tissue Processing

To induce acute or chronic demyelination, male mice (19–21g) were intoxicated with 0.25% cuprizone (bis(cyclohexanone)oxaldihydrazone, Sigma-Aldrich, St. Louis, MO, USA) mixed into ground standard rodent chow (Ssniff, Soest, Germany) for five or 12 weeks, respectively. Control groups were fed with cuprizone-free standard rodent chow. Detailed numbers of animals used for the different experiments are provided in the figure legends. After five or 12 weeks, the animals were perfused with ice-cold phosphate-buffered saline (PBS) followed by a 3.7% formaldehyde solution (pH 7.4). After overnight post-fixation in the same fixative, brains were carefully removed from the

skull and processed for paraffin embedding or cryoprotection following established protocols [12,32]. For the preparation of paraffin sections, the brains were dehydrated, cleared with xylene, embedded in paraffin, and cut into 5- μ m-thick coronal sections using a sliding microtome (Type SM 2000R; Leica Microsystems, Wetzlar, Germany). To prepare cryo-sections, post-fixed brains were rinsed in PBS and cryoprotected in sucrose solutions (10%, 20%, and finally 30% sucrose (*w/v*) in PBS) at 4 °C for 24 h in each solution. Thereafter, brains were frozen in isopentane (−70 °C, 1 min) on dry ice, cut into 40- μ m-thick coronal serial sections on a cryostat (Type CM 1950; Leica Microsystems), and stored at −20 °C in a cryoprotective solution (30% ethylene glycol, 30% glycerol in PBS) until further processing.

For immunohistochemical analyses of paraffin sections, two consecutive sections (level R265 according to Reference [33]) were processed as previously described [34]. In brief, sections were deparaffinized, rehydrated, heat-unmasked by Tris–ethylene diamine tetraacetic acid (EDTA) (pH 9.0) and blocked in 5% normal goat serum or a mixture of 2% normal goat serum, 0.1% cold water fish skin gelatin, 1% bovine serum albumin, and 0.05% Tween-20. Sections were incubated with the following primary antibodies overnight at 4 °C: myelin proteolipid protein (PLP), 1:5000, RRID:AB_2237198, Bio-Rad, Hercules, CA, USA; ionized calcium-binding adapter molecule 1 (IBA1), 1:5000, RRID:AB_2665520, Wako, Neuss, Germany; amyloid precursor protein (APP), 1:5000, RRID:AB_94882, Merck-Millipore, Burlington, VT, USA. On the next day, sections were treated with 0.3% hydrogen peroxide in PBS, and the biotinylated secondary antibodies (goat anti-mouse immunoglobulin G (IgG), goat anti-rabbit IgG, 1:200; Vector labs, Burlingame, CA, USA) were applied for 1 h. Thereafter, sections were incubated in peroxidase-coupled avidin–biotin reagent (ABC kit, Vector labs) and the antigen–antibody complexes were finally visualized by 3,3'-diaminobenzidine (Dako, Hamburg, Germany). Sections were counterstained with standard hematoxylin to visualize cell nuclei if appropriate.

For stereological analyses of cryostat sections, every third section between levels R265 and R305 (according to Reference [33]; Figure 1) was selected with a random start (first series). In these regions, demyelination can be induced in a highly reproducible manner in the corpus callosum [35,36]. Demyelination is not only restricted to this white-matter tract but also involves other brain areas including the cerebral cortex, basal ganglia, and thalamus [23,37,38]. Sections were mounted on gelatinized glass slides, dried, and stained with cresyl violet (Nissl staining) [39]. For a second series of sections (every sixth section), free-floating immunofluorescence staining was performed. Sections were blocked in blocking solution (10% normal donkey serum/0.5% Triton X-100/PBS) and incubated with the primary antibodies (NeuN, 1:2000, RRID:AB_2298772, Merck-Millipore) for 48 h at 4 °C. Thereafter, sections were incubated with the secondary antibodies (donkey anti-mouse Alexa Fluor 488, 1:500; Life Technologies, Carlsbad, CA, USA) for 6 h. Cell nuclei were counterstained using DAPI (4,6-diamidino-2-phenyl-indole; Life Technologies), and sections were mounted on gelatinized glass slides and coverslipped using FluorPreserve reagent (Merck-Millipore).

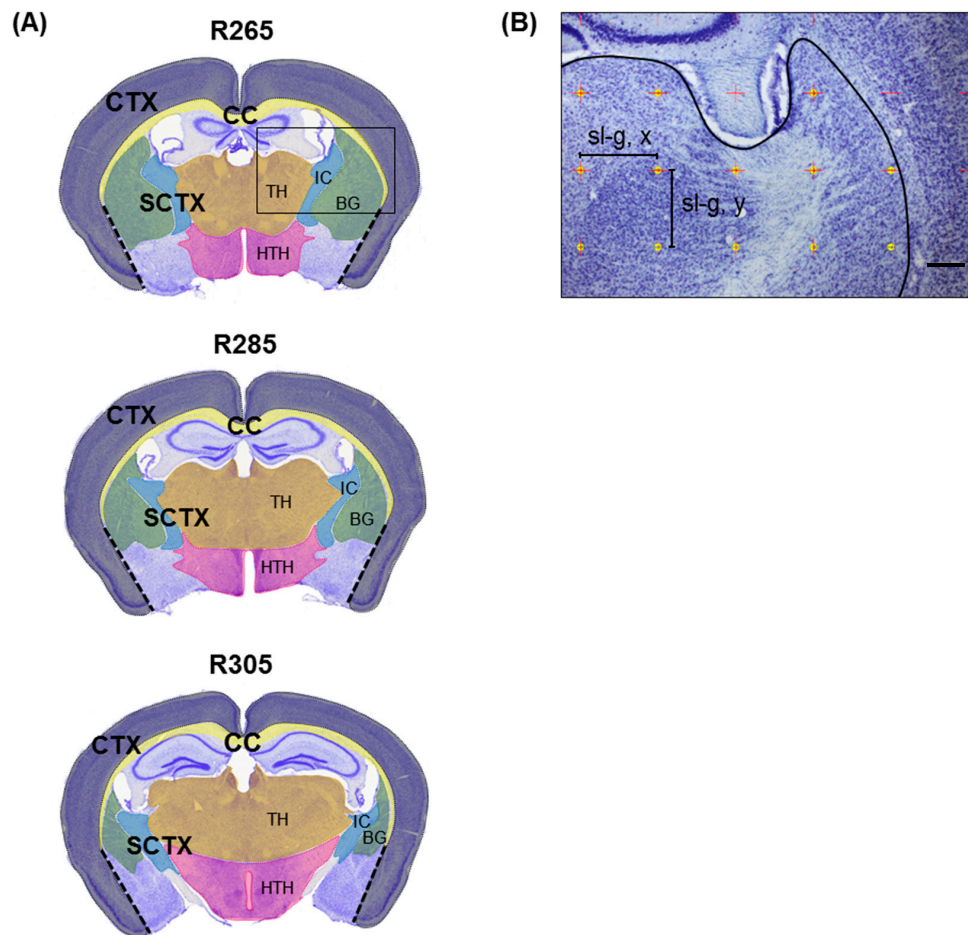


Figure 1. (A) Representative coronal sections of a mouse brain at levels R265, R285, and R305 (according to Reference [33]) showing regions investigated in the present study (corpus callosum (CC, yellow); cerebral cortex (CTX, gray); thalamus (TH, brown); hypothalamus (HTH, pink); internal capsule (IC, blue); basal ganglia (BG, green)). (B) Representative photomicrograph of a Nissl-stained coronal section (enlarged view of black square in (A)). The slide is superimposed with a rectangular grid (intersections are represented by red crosses; sl-g = side length in x - and y -directions of the grid) to estimate the volume of the designated areas. Grid intersections within the subcortical area are highlighted as yellow dots. Scale bar in (B) = 1 mm (A) and 200 μm (B).

2.3. Evaluation of Histological Parameters and Stereological Analysis

To validate demyelination and microgliosis in the cuprizone model, two consecutive (PLP- and IBA1-stained) sections per mouse were evaluated by densitometry of the staining intensity, and the results were averaged. Staining intensity of the region of interest (ROI) was quantified using ImageJ (NIH, version 1.47v, Bethesda, MD, USA) and is given as percentage myelination or percentage area of the entire ROI. For quantification of axonal damage, APP⁺ spheroids were counted as previously described [23]. In general, densities are given in spheroids or cells per square millimeter (mm^2).

Stereological analyses were performed with the stereology software (Stereo Investigator, version 11.07; MBF Bioscience, Williston, ND, USA) and either a light microscope (Olympus BX51WI; Olympus, Tokyo, Japan) equipped with a motorized specimen stage (MBF Bioscience), UPlanApo objective (4 \times , numerical aperture (N.A.) = 0.16; Olympus), and a charge-coupled device (CCD) color video camera (U-CMAD-2; Olympus) or a modified fluorescence microscope (Olympus BX51; Olympus) equipped with a motorized specimen stage (MBF Bioscience), a customized spinning disk unit (DSU;

Olympus), UPlanSApo objective (20×, N.A. = 0.75; Olympus), Alexa Fluor 488 filter (excitation: 498 nm, emission: 520 nm; Chroma, Bellows Falls, VT, USA), and a Retiga 2000R CCD camera (Q-Imaging, Surrey, BC, Canada).

The first series of sections was stained with cresyl violet to analyze the volumes of the selected brain regions. The volumes of the distinct brain regions (cerebral cortex, subcortical area, corpus callosum, internal capsule, hypothalamus, thalamus, and basal ganglia (globus pallidus and caudoputamen)) were calculated using Cavalieri's principle [40]. Areas of brain regions were determined by tracing their boundaries on each section using the stereology software. Medial boundaries of the cortex (CTX) were defined by the corpus callosum and a line drawn between the basal tip of the corpus callosum and the basal end of the piriform area (shown in Figure 1A as dashed line). The thalamus, hypothalamus, basal ganglia, and internal capsule were summed up as the subcortical area (SCTX). To estimate the volume of the distinct brain regions, the slides were superimposed by a rectangular grid (Figure 1B, Table 1). Then, the volumes of brain regions were calculated by summing the counted points (grid intersections) from all sections (Table 1) and multiplying this value with the area associated with each point, the section interval, and the average cut section thickness.

Table 1. Details of the stereological estimation procedure.

	CC	CTX	SCTX	TH	HTH	BG	IC
sl-g (μm)	220	500	500	120	120	120	120
Σpoints _{area}	337	669	985	5693	3192	2205	1943
sl-uvf (μm)	-	35	35	-	-	-	-
B (μm ²)	-	1225	1225	-	-	-	-
H (μm)	-	15	15	-	-	-	-
D (μm)	-	1100	1100	-	-	-	-
ΣUVCS	-	155	185	-	-	-	-
Σneurons	-	653	555	-	-	-	-
sl-g (μm)	-	-	400	-	-	-	-
Σpoints _{perikarya}	-	-	305	-	-	-	-
Σpoints _{neuropil}	-	-	526	-	-	-	-

Details for stereological analysis of the corpus callosum (CC), cerebral cortex (CTX), subcortical area (SCTX), thalamus (TH), hypothalamus (HTH), basal ganglia (BG), and internal capsule (IC): sl-g = side length in *x*- and *y*-directions of the grids used to determine the volume; Σpoints = mean number of counted points per animal; sl-uvf = side length in *x*- and *y*-directions of unbiased counting frames; B and H = base and height of the unbiased virtual counting spaces; D = distances between the unbiased virtual counting spaces in *x*- and *y*-directions; ΣUVCS = mean number of unbiased virtual counting spaces per animal; Σneurons = mean number of counted neurons per animal.

The second series of sections was stained with anti-NeuN antibodies to analyze total neuronal numbers and densities within the distinct brain regions using the optical fractionator method [40,41]. The base of the unbiased virtual counting spaces (UVCS) was 1225 μm², the height was 15 μm, and the upper guard zone was 4 μm. The distance between the UVCS in *x*- and *y*-directions was 1100 μm and 1100 μm, respectively (Table 1). All neurons whose nucleus top came into focus within the UVCS were counted. Then, total neuronal numbers were calculated from the numbers of marked neurons (Table 1) and the corresponding sampling probability. Neuronal densities were calculated as the ratio of total numbers of neurons and the volume (measured section thickness × sum of all cross-sectional areas) of the region. The fractional volumes occupied by NeuN immunoreactive perikarya or the neuropil in the SCTX were estimated by counting randomly positioned test points (grid intersections) falling on nerve cell perikarya or the neuropil according to Cavalieri's principle.

2.4. [¹⁸F]-Fluoro-2-deoxy-D-glucose Positron-Emission Tomography (FDG PET) Imaging

Chronic cuprizone-intoxicated mice (12 weeks of cuprizone) and controls were imaged with [¹⁸F]-FDG-PET on the last day of treatment. Then, μPET imaging followed a standardized protocol [42]. In brief, 12.4 ± 2.1 MBq [¹⁸F]-FDG was injected into the tail vein after a fasting period >3 h. Emission

was acquired from 30 to 60 min post injection followed by a 15-min transmission scan. All images were co-registered to a [^{18}F]-FDG-PET mouse template and normalized to standardized uptake values (SUV). Predefined brain regions of the Mirrione mouse atlas implemented in PMOD v3.5 (PMOD technologies, Basel, Switzerland) were applied to extract individual regional glucose metabolism of all studied mice. Averaged SUV images of chronic cuprizone-intoxicated mice and control mice were used to calculate voxel-based percentage changes between both groups.

2.5. Statistical Analyses

For each group of animals, data are presented as individual values and means per group. Data were firstly analyzed using the Kolmogorov–Smirnov test for normality. Differences between groups were then analyzed using Student's *t*-test or the Mann–Whitney U test, as appropriate. Data were not corrected for multiple comparisons. The *p*-values and the applied statistical procedures are given in the respective figure legends. A *p*-value <0.05 was considered to be statistically significant. Calculations were performed using GraphPad Prism (GraphPad Software Inc., version 5.04; San Diego, CA, USA).

3. Results

3.1. Acute Demyelination Does Not Lead to Brain Volume Loss

We firstly investigated the severity of acute cuprizone-induced injury (i.e., demyelination, microglia activation, and axonal damage) in the different brain regions. To this end, animals were intoxicated with cuprizone for five weeks, and myelination (anti-PLP), microgliosis (anti-IBA1), and acute axonal damage (anti-APP) were compared to controls which were fed normal chow during the experimental period. In line with previous findings [23,34,36,43,44], immunohistochemical analyses revealed extensive demyelination of the medial corpus callosum, the cerebral cortex, and the subcortical area after five weeks of cuprizone intoxication (Figure 2A). Demyelination was most severe in the corpus callosum, followed by the cerebral cortex and the subcortical area. In the corpus callosum and the subcortical area, acute demyelination was paralleled by increased microglia densities (Figure 2B), in line with previous results from our group [23,36]. In the cerebral cortex, microglia activation was less severe, but IBA1⁺ cells clearly showed an activated phenotype (swollen cell bodies and retracted processes; see Figure 2B). To examine the extent of acute axonal damage, we quantified APP⁺ spheroids, a marker of acute axonal injury. As shown in Figure 2C, numerous APP⁺-spheroids were found in the corpus callosum, the cerebral cortex, and the subcortical area of cuprizone-intoxicated animals. Such spheroids were not observed in control animals.

Furthermore, we investigated whether acute cuprizone-induced injury results in overall brain volume changes in the analyzed region (R265–R305). Mean overall volume was not altered in cuprizone-intoxicated versus control mice (control (Co): 63.68 mm³ ± 1.15 mm³; cuprizone (Cup): 64.34 mm³ ± 0.89 mm³; *p* = 0.076). Furthermore, we measured the volume of the corpus callosum, the cerebral cortex, and the subcortical area by stereological analysis. Despite extensive demyelination and axonal damage, individual brain volumes for the corpus callosum, cortex, and subcortical area were comparable in control and five weeks of cuprizone-intoxicated mouse brains (Figure 2D).

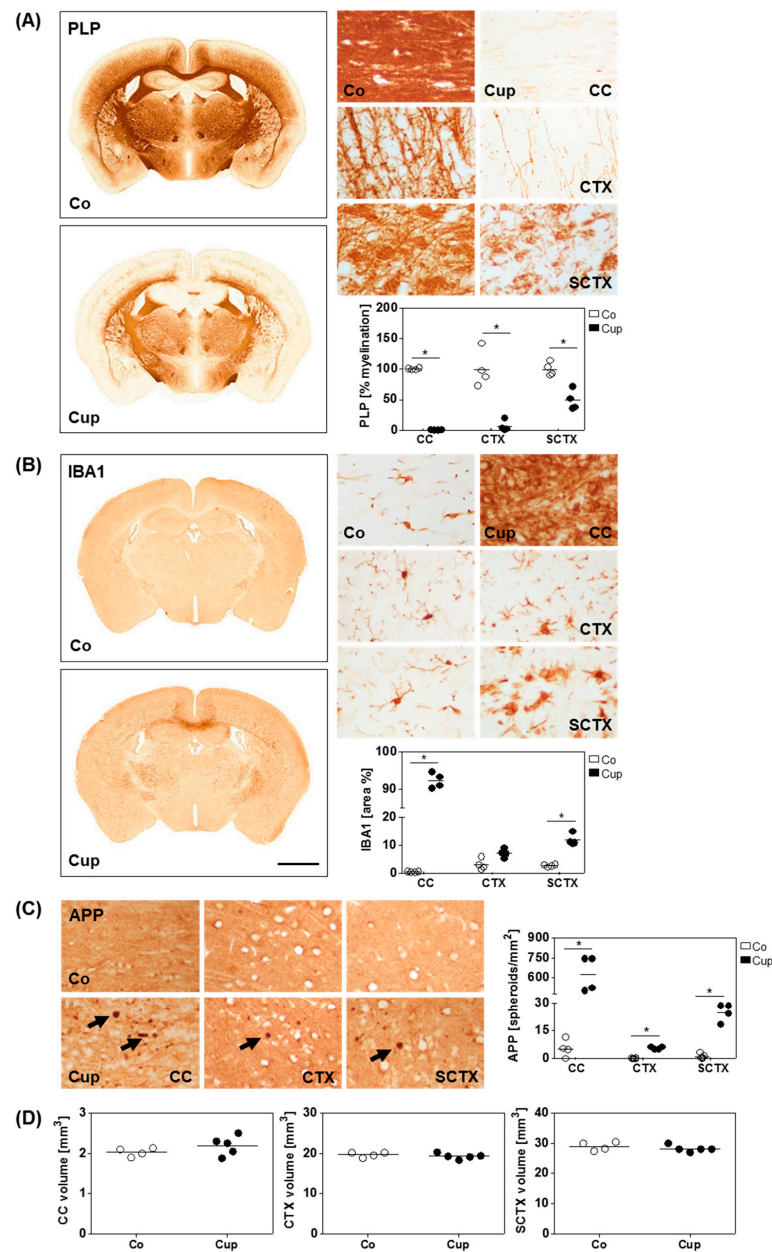


Figure 2. Acute demyelination does not lead to volumetric changes. **(A)** Quantification of myelination (anti-myelin proteolipid protein (PLP)) and **(B)** microgliosis (anti-ionized calcium-binding adapter molecule 1 (IBA1)) from controls (Co) ($n = 4$) and five weeks of cuprizone-intoxicated (Cup) mice ($n = 4$). Individual brain regions are shown in higher magnification: medial corpus callosum (CC), cortex (CTX), and subcortical area (SCTX). **(C)** Quantification of axonal damage (anti-amyloid precursor protein (APP)) with representative pictures of the medial CC, CTX, and SCTX from Co and Cup mice. Arrows indicate APP⁺ spheroids. **(D)** Volumes of the CC, CTX, and the SCTX of Co ($n = 4$) and Cup mice ($n = 5$), analyzed with design-based stereology. Data are shown as individual values and means per group (lines). Statistical analysis revealed significant differences between Co and Cup in **(A)** (CC, $p = 0.03$, CTX, $p = 0.03$, SCTX, $p = 0.03$), **(B)** (CC, $p = 0.03$; SCTX, $p = 0.03$), and **(C)** (CC, $p = 0.02$, CTX, $p = 0.02$, SCTX, $p = 0.02$); * $p < 0.05$. Scale bar in **(B)** = 2 mm (**A,B**) and 17 μm (enlarged views (**A,B**) and **(C)**).

3.2. Chronic Demyelination Results in Regional Brain Volume Loss

In a next step, we investigated histopathological changes after chronic cuprizone intoxication. Therefore, mice were fed with cuprizone for 12 weeks, and myelination and microglia activation were evaluated. As shown in Figure 3A, severe loss of anti-PLP staining intensity was evident in several brain regions, including the corpus callosum and cerebral cortex of animals intoxicated for 12 weeks. Moreover, moderate but consistent demyelination was observed in the subcortical area. Of note, chronic demyelination was paralleled by increased microglia densities (Figure 3B). To analyze volumetric changes after chronic demyelination, we analyzed the overall brain volume (R265–R305). The overall volume of cuprizone-intoxicated mice was significantly smaller compared to control mice (Co: $67.16 \text{ mm}^3 \pm 0.66 \text{ mm}^3$; Cup: $65.28 \text{ mm}^3 \pm 0.38 \text{ mm}^3$; $p = 0.045$). Next, we measured the individual brain volumes after chronic cuprizone-induced demyelination. Mean volumes of the corpus callosum and the subcortical area were significantly smaller in cuprizone-intoxicated versus control mice. In particular, the volume of the corpus callosum was $1.96 \text{ mm}^3 \pm 0.10 \text{ mm}^3$ in control, and $1.59 \text{ mm}^3 \pm 0.09 \text{ mm}^3$ in cuprizone-intoxicated mice ($p = 0.02$), whereas the volume of the subcortical area was $30.96 \text{ mm}^3 \pm 0.34 \text{ mm}^3$ in control, and $29.11 \text{ mm}^3 \pm 0.14 \text{ mm}^3$ in cuprizone-intoxicated mice ($p = 0.0012$). No volume loss was observed in the cortex (Figure 3C).

As demonstrated above, a volume reduction after chronic cuprizone-induced demyelination was found in the subcortical area, which consists of distinct white- and gray-matter areas including different functional nuclei. Next, we were interested which subcortical region is most vulnerable in the cuprizone model. Thus, we decided to separately evaluate the volumes of the thalamus, hypothalamus, basal ganglia, and the internal capsule, and contrast atrophy with the extent of demyelination. As demonstrated in Figure 3D, anti-PLP staining intensities were clearly reduced in the thalamus, hypothalamus, and basal ganglia, yet demyelination was incomplete. In contrast, loss of anti-PLP staining intensity was moderate in the internal capsule (Figure 3D). Volumetric measurements revealed that the mean volumes of the internal capsule and the thalamus were significantly lower in cuprizone-intoxicated versus control mice. In particular, the volume of the internal capsule was $3.60 \text{ mm}^3 \pm 0.14 \text{ mm}^3$ in control, and $3.08 \text{ mm}^3 \pm 0.14 \text{ mm}^3$ in cuprizone-intoxicated mice ($p = 0.04$), whereas the volume of the thalamus was $10.18 \text{ mm}^3 \pm 0.24 \text{ mm}^3$ in control, and $9.45 \text{ mm}^3 \pm 0.20 \text{ mm}^3$ in cuprizone-intoxicated mice ($p = 0.02$). In contrast, the mean hypothalamus and basal ganglia volumes were not found to be reduced after chronic demyelination (Figure 3E).

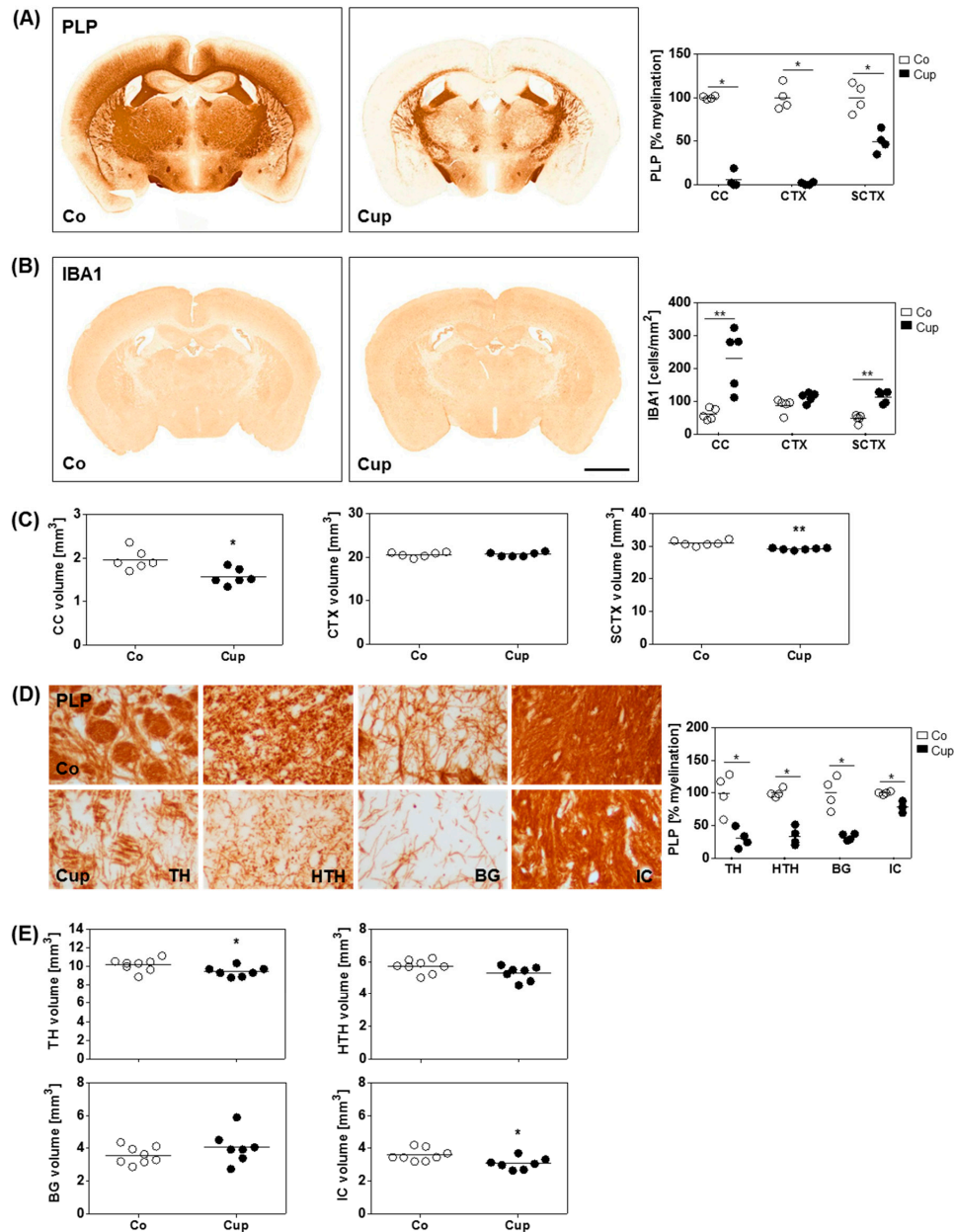


Figure 3. Chronic demyelination leads to subcortical volumetric reduction. **(A)** Quantification of myelination (anti-PLP) and **(B)** microgliosis (anti-IBA1) in the medial corpus callosum (CC), cortex (CTX), and subcortical area (SCTX) from controls (Co) ($n = 4$) and five weeks of cuprizone-intoxicated (Cup) mice ($n = 5$). **(C)** Volumes of the CC, CTX, and the SCTX of Co ($n = 6$) and Cup mice ($n = 6$) analyzed with design-based stereology. **(D)** Quantification of myelination with representative pictures of individual subcortical regions (thalamus (TH), hypothalamus (HTH), basal ganglia (BG), internal capsule (IC)) from Co ($n = 4$) and Cup mice ($n = 4$). **(E)** Volumes of the TH, HTH, STR, and IC of Co ($n = 8$) and Cup mice ($n = 7$). Data are shown as individual values and means per group (lines). Statistical analysis revealed significant differences between Co and Cup in **(A)** (CC, $p = 0.03$, CTX, $p = 0.03$, SCTX, $p = 0.03$), **(B)** (CC, $p = 0.008$; SCTX, $p = 0.008$), **(C)** (CC, $p = 0.02$; SCTX, $p = 0.0012$), **(D)** (TH, $p = 0.03$; HTH, $p = 0.03$; BG, $p = 0.03$; IC, $p = 0.03$), and **E** (TH, $p = 0.04$; IC, $p = 0.02$); * $p < 0.05$, ** $p < 0.01$. Scale bar in **(B)** = 2 mm (**A,B**) and 17 μm (**D**).

3.3. Axonal Damage Rather Than Neuronal Loss Contributes to Brain Volume Loss

To investigate whether the observed subcortical volume reduction results from (i) neuronal cell body loss and/or (ii) acute axonal damage, we firstly quantified the mean numbers of neurons and mean densities of neurons in the cerebral cortex and the entire subcortical area using design-based stereology. In the cerebral cortex, no alterations in mean neuronal numbers and mean neuronal densities were detected in 12 weeks of cuprizone-intoxicated mice (Figure 4A,B). Of note, also in the subcortical area, the mean numbers and densities of neurons were comparable in 12 weeks of cuprizone-intoxicated mice as compared to age-matched controls (Figure 4A,B). Furthermore, in the entire subcortical area, the space occupied by perikarya and the neuropil was not significantly different in cuprizone-intoxicated versus control mice (Figure 4C).

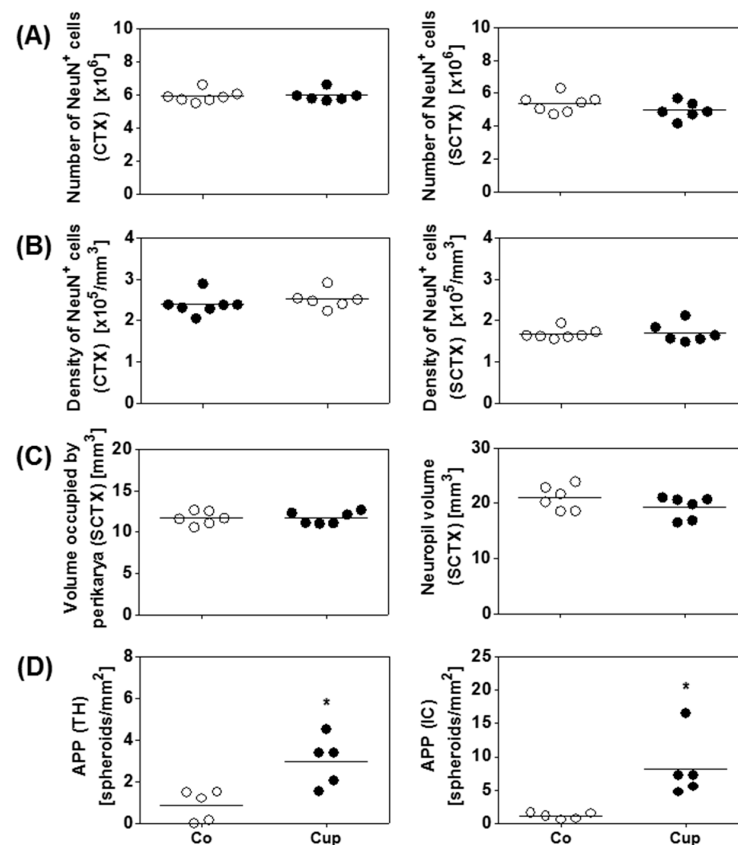


Figure 4. Effects of chronic demyelination on the neuro-axonal/-dendritic compartment. (A) Numbers and (B) densities of neurons in the cerebral cortex (CTX) and the subcortical area (SCTX) of control (Co) ($n = 6$) and 12 weeks of cuprizone-intoxicated (Cup) mice ($n = 6$) analyzed with design-based stereology. (C) Neuropil volumes and volumes occupied by nerve cell perikarya in the SCTX of Co ($n = 6$) and 12-week Cup mice ($n = 6$). (D) Quantification of amyloid precursor protein (APP)-positive spheroids in the thalamus (TH) and internal capsule (IC) of chronically demyelinated mice ($n = 5$). Data are shown as individual values and means per group (lines). Statistical analysis revealed significant differences between Co and Cup in (D) (TH, $p = 0.02$; IC, $p = 0.02$); * $p < 0.05$.

Secondly, we investigated the densities of APP⁺ spheroids. We focused in this part of the study on the thalamus and the internal capsule because volume loss was found to be most severe in these two subcortical brain areas. As shown in Figure 4D, numerous APP⁺ spheroids were found in the thalamus and the internal capsule of 12 weeks of cuprizone-intoxicated mice. Such spheroids were not observed in control animals (Figure 4D).

3.4. Mice with Chronic Demyelination Show Higher Uptake of [^{18}F]-FDG in the Thalamus

Neuroimaging is a central part of the diagnostic work-up of patients with suspected neurodegenerative disease, including MS. [^{18}F]-FDG PET is an attractive tool to study neurodegeneration on the metabolic level. Therefore, we were interested whether we could detect metabolic alterations after chronic demyelination. To this end, glucose metabolism in the mouse brain was analyzed using [^{18}F]-FDG μPET . Interestingly, we found a region-dependent increase of [^{18}F]-FDG uptake in cuprizone-treated mice. A visual interpretation of the [^{18}F]-FDG μPET scans indicated increased [^{18}F]-FDG μPET signal, particularly in the subcortical area (Figure 5A,B). A statistical comparison between predefined brain regions in the control and cuprizone-intoxicated mice showed significantly higher [^{18}F]-FDG uptake in the thalamus of 12 weeks of cuprizone-intoxicated mice (increase of 22%). There were no significant differences in [^{18}F]-FDG uptake in the cortex, hypothalamus, and basal ganglia in 12 weeks of cuprizone-intoxicated mice compared to age-matched controls (Figure 5C).

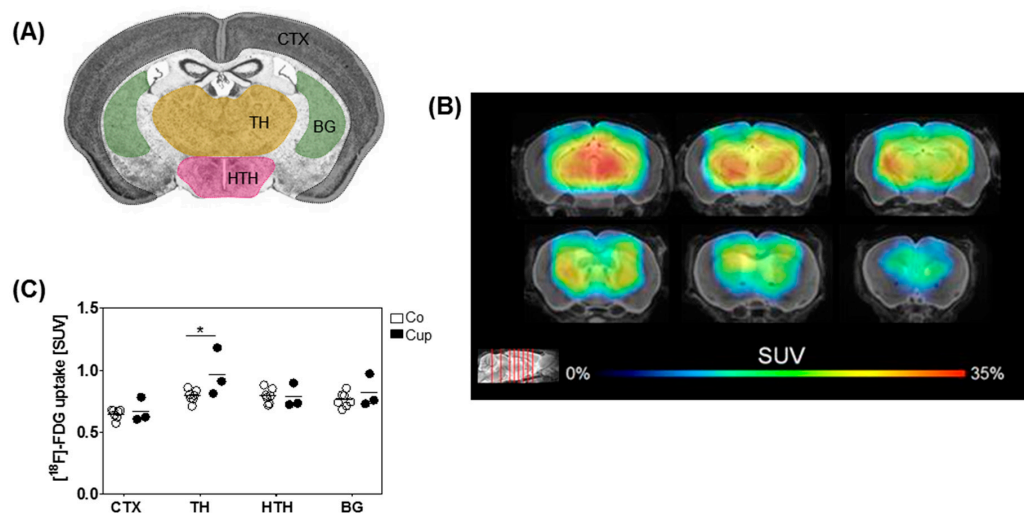


Figure 5. Altered [^{18}F]-fluoro-2-deoxy-D-glucose ([^{18}F]-FDG) ligand uptake after chronic cuprizone intoxication. (A) Schematic illustration of the different brain regions (cortex (CTX), thalamus (TH), hypothalamus (HTH), and basal ganglia (BG)), evaluated for [^{18}F]-FDG ligand uptake. (B) Cumulative heat map illustrating percentage increases of standardized uptake values (SUV) in cuprizone-treated mice relative to controls. (C) Quantification of the normalized [^{18}F]-FDG uptake in Co ($n = 7$) and 12-week Cup mice ($n = 3$). Data are shown as individual values and means per group (lines). Statistical analysis revealed significant differences between Co and Cup in (C) (TH, $p = 0.03$); $*p < 0.05$.

4. Discussion

This is the first study focusing on volume, neuronal densities, and total neuronal numbers in the cerebral cortex and subcortical area after acute and chronic cuprizone-induced demyelination. We could show that specific subregions display volume loss after chronic cuprizone-induced demyelination, particularly the corpus callosum, internal capsule, and the thalamus. Of note, volumetric changes were not paralleled by loss of NeuN $^{+}$ neuronal cell numbers or shrinkage of their perikarya, but by ongoing degeneration of axons, as demonstrated by the ongoing axonal transport deficit of APP.

Of note is the specific volume loss of the subcortex, whereas no significant volumetric changes were observed in the cerebral cortex. It is well known that, in addition to the corpus callosum, the cortex is a vulnerable brain region in the cuprizone model, demonstrating severe and almost complete demyelination after a five-week cuprizone intoxication period [37,45]. It was, therefore, somewhat surprising that we did not detect cortical atrophy in the cortex even after chronic cuprizone exposure. Since we only evaluated the entire cortex, we cannot rule out that specific cortical subregions, such

as the somatosensory and somatomotor cortex, which are particularly vulnerable in the cuprizone model, show reduced volumes [24]. While axonal damage/injury was observed by many groups in the cuprizone model [11,12,30], a decrease in neuronal densities or neuronal cell numbers is less well appreciated. While Tiwari-Woodruff's lab demonstrated a loss of parvalbumin-expressing interneurons in the hippocampal CA1 region [29], Löscher's lab showed a loss of neurons in the hilus of the dentate gyrus [30]. While neuronal cell loss in the MS brain clearly exists [46], it is unclear which mechanisms trigger neurodegeneration. In the cuprizone model, demyelination alone seems not to be sufficient to trigger neuronal cell loss, at least in the investigated brain areas. Interestingly, recent post-mortem studies did not reveal any association between the extent of demyelination and the density of neurons in the MS neocortex [47,48]. We speculate that, in addition to metabolic stressors, auto-immune driven inflammatory mediators are necessary to induce neuronal cell loss in the neocortex and, consequently, cortical brain atrophy. A recently described novel MS animal model principally allows studying the interplay of innate and adaptive immunity [49–51], and we are currently investigating in ongoing studies the extent to which the liaison of metabolic and inflammatory brain injury triggers neuronal degeneration.

We are well aware that the underlying mechanisms of MS and cuprizone-induced injury are most likely not the same. Nevertheless, several important aspects of the MS pathology are nicely recapitulated by the cuprizone model. For example, mitochondrial density is increased within demyelinated axons in active MS [52] and cuprizone-induced lesions [53]. Furthermore, splitting of the inner myelin lamella, referred as dying-back oligodendroglialopathy, was reported in MS [54] and cuprizone-induced demyelination [55]. Finally, the presence of apoptotic oligodendrocytes, which express active caspase-3 during lesion formation, was described in MS [56] and the cuprizone model [57]. Thus, understanding mechanisms operant during cuprizone-induced demyelination might help to understand disease mechanisms in MS.

As pointed out above, significant brain volume loss was found in subcortical regions among the thalamus (see Figure 3E). The thalamus forms the largest part of the diencephalon and is eponymous for other diencephalic components such as the epithalamus and hypothalamus. This diencephalic brain region is highly interconnected with various cortical and subcortical areas. We speculate that the thalamus with its multiple reciprocal connections is sensitive to pathological processes occurring in different brain regions, thus acting as a “barometer” for diffuse brain parenchymal damage in MS [58]. Our findings are in line with a specific subcortical gray-matter atrophy found in MS patients [19,20,59,60]. In these MRI studies, subcortical gray-matter atrophy was most prominent in the thalamus, showing a volume reduction of 12–25%. From a functional point of view, it is interesting to note that the thalamus volume loss strongly correlated to patients' declining cognitive functions and physical disability [19,20,61,62], highlighting the thalamus as a central structure in the context of MS-related disability and disease progression.

Thalamic volume loss was found to be related to neuro-axonal pathology. Cifelli et al. found a reduction in both neuronal densities and *N*-acetylaspartate (NAA) concentration in the thalamus of MS patients [60]. In the present study, cuprizone-induced demyelination neither affected NeuN⁺ neuronal numbers and densities nor the space occupied by perikarya. Noteworthy, our [¹⁸F]-FDG-PET measurements indicated a significant hypermetabolism in the thalamus of cuprizone-intoxicated mice when compared to controls, fitting to preserved neuronal numbers in this brain region, as the vast majority of the [¹⁸F]-FDG-PET signal is supposed to be related to neuronal energy metabolism [63]. Thus, it seems likely that equal neuronal numbers, together with increased glial activity after chronic cuprizone intoxication, will result in higher net energy consumption when compared to controls. Of note, there is still no evidence how much glial cells contribute to the cerebral energy consumption, although it is assumed that glucose metabolism decreases when microglia are dysfunctional [64].

Surprisingly, we did not find callosal volume loss after acute cuprizone-induced demyelination, despite significant axonal injury. This could have happened for a number of reasons. Firstly, in our study, we did not measure irreversible axonal degeneration or axonal loss, but rather a deficit

of the anterograde axonal transport machinery. The gold-standard method to detect axonal loss is electron microscopy or thin plastic sections. Most previous studies which analyzed acute axonal injury in the cuprizone model visualized either axonal transport deficits or the expression changes of neurofilament proteins [11,65], which does not necessarily represent the true extent of irreversible axonal degeneration [66]. Secondly, due to the severe astrogliosis and microgliosis accompanying the cuprizone-induced demyelination, callosal volume loss might be “masked” despite axonal loss (if present). Thirdly, cuprizone intoxication results in spongy degeneration of the white matter [67], another pathological feature which might mask callosal volume loss. In MS, it was suggested that untreated inflammation and edema might increase the brain volume, leading to an underestimation of true tissue loss. Interestingly, anti-inflammatory therapies were associated with acceleration of brain volume loss, referred to as pseudoatrophy [68]. This is likely caused by the resolution of inflammation and edema rather than true brain atrophy. In our study, chronic cuprizone-induced demyelination did lead to a brain volume reduction despite ongoing microgliosis, suggesting true tissue loss. Furthermore, it was suggested that pseudoatrophy effects are greater in white-matter structures due to larger glial infiltration and activation compared to gray-matter structures. Thus, volume measurement of gray-matter structures might be more reliable to distinguish irreversible changes due to tissue loss from the reversible changes due to pseudoatrophy. The pathological substrate of subcortical volume loss in the cuprizone model is currently unknown. In principle, volume loss might be due to loss of the myelin sheath (i.e., demyelination), glia degeneration, neuronal cell loss, axonal degeneration, or synaptic pathology. Of note, in a post mortem analysis, widespread loss of dendritic spines was found in the cortex of MS patients. Dendritic spine loss occurred in demyelinated and non-demyelinated cortex regions, and preceded loss of cortical axons [69]. In this study, we could show that subcortical volume loss is not paralleled by a reduction of total neuronal cell numbers. However, subcortical neuropil volumes tended to decrease, suggesting degeneration in the axonal and/or dendritic compartment. Of note, in this study, we did not quantify the loss of cell types other than neurons, such as astrocytes or oligodendrocytes, by means of design-based stereology. It, thus, might well be that the observed atrophy in the thalamus, for example, is due to oligodendrocyte or astrocyte degeneration. In a recent study, we were able to show that astrocytes express the stress-associated transcription factor DNA damage-inducible transcript 3 after acute cuprizone-induced demyelination [32]. Further studies are needed to investigate this aspect in more detail.

As already pointed out above, the thalamus shares broad reciprocal connections with other brain regions, such as the cerebral cortex. These connections run within the internal capsule. In the present study, we observed volume reduction and axonal damage of the internal capsule, despite moderate demyelination. Thus, volume loss of the internal capsule might be due to the degeneration of efferent thalamic fiber tracts. This is consistent with findings demonstrating reduced NAA levels in normal-appearing white matter of the internal capsule in MS patients [70].

In summary, this study pointed out that the chronic, but not the acute cuprizone model may serve as a valuable tool to study subcortical brain volume loss. Further studies are now warranted to investigate which mechanisms are operant and how this brain volume loss can be ameliorated by pharmacological intervention.

Author Contributions: Conceptualization, T.H. and M.K.; formal analysis, T.H., S.R., K.H., and K.H.F.; investigation, T.H., S.R., K.H., K.H.F., U.C., F.E., and C.S. (Christian Sacher); methodology, T.H., M.B., C.S. (Christoph Schmitz), and M.K.; supervision, M.K.; visualization, T.H.; writing—original draft, T.H. and S.R.; writing—review and editing, M.B., C.S. (Christoph Schmitz), and M.K.

Acknowledgments: The authors thank Sarah Wübbel, Beate Aschauer, Astrid Baltruschat, and Barbara Mosler for their excellent and valuable technical assistance. The authors gratefully acknowledge Maren Kiessling for her valuable input regarding the stereological evaluation.

Conflicts of Interest: The authors declare no conflicts of interest.

References

1. Trapp, B.D.; Nave, K.A. Multiple sclerosis: An immune or neurodegenerative disorder? *Annu. Rev. Neurosci.* **2008**, *31*, 247–269. [[CrossRef](#)] [[PubMed](#)]
2. Rovaris, M.; Confavreux, C.; Furlan, R.; Kappos, L.; Comi, G.; Filippi, M. Secondary progressive multiple sclerosis: Current knowledge and future challenges. *Lancet Neurol.* **2006**, *5*, 343–354. [[CrossRef](#)]
3. Rudick, R.; Bö, L.; Trapp, B.D.; Peterson, J.; Ransohoff, R.M.; Mörk, S. Axonal Transection in the Lesions of Multiple Sclerosis. *New Engl. J. Med.* **1998**, *338*, 278–285.
4. Grimaud, J.; Barker, G.J.; Wang, L.; Lai, M.; MacManus, D.G.; Webb, S.L.; Thompson, A.J.; McDonald, W.I.; Tofts, P.S.; Miller, D.H. Correlation of magnetic resonance imaging parameters with clinical disability in multiple sclerosis: A preliminary study. *J. Neurol.* **1999**, *246*, 961–967. [[CrossRef](#)] [[PubMed](#)]
5. Calabrese, M.; Romualdi, C.; Poretto, V.; Favaretto, A.; Morra, A.; Rinaldi, F.; Perini, P.; Gallo, P. The changing clinical course of multiple sclerosis: A matter of gray matter. *Ann. Neurol.* **2013**, *74*, 76–83. [[CrossRef](#)] [[PubMed](#)]
6. Oh, J.; O'Connor, P.W. Established disease-modifying treatments in relapsing-remitting multiple sclerosis. *Curr. Opin. Neurol.* **2015**, *28*, 220–229. [[CrossRef](#)] [[PubMed](#)]
7. Wingerchuk, D.M.; Carter, J.L. Multiple Sclerosis: Current and Emerging Disease-Modifying Therapies and Treatment Strategies. *Mayo Clin. Proc.* **2014**, *89*, 225–240. [[CrossRef](#)]
8. Simmons, S.B.; Pierson, E.R.; Lee, S.Y.; Goverman, J.M. Modeling the Heterogeneity of Multiple Sclerosis in Animals. *Trends Immunol.* **2013**, *34*, 410–422. [[CrossRef](#)]
9. Patel, J.; Balabanov, R. Molecular Mechanisms of Oligodendrocyte Injury in Multiple Sclerosis and Experimental Autoimmune Encephalomyelitis. *Int. J. Mol. Sci.* **2012**, *13*, 10647–10659. [[CrossRef](#)]
10. Rossi, B.; Constantin, G. Live Imaging of Immune Responses in Experimental Models of Multiple Sclerosis. *Front. Immunol.* **2016**, *7*. [[CrossRef](#)]
11. Hoflich, K.M.; Beyer, C.; Clarner, T.; Schmitz, C.; Nyamoya, S.; Kipp, M.; Hochstrasser, T. Acute axonal damage in three different murine models of multiple sclerosis: A comparative approach. *Brain Res.* **2016**, *1650*, 125–133. [[CrossRef](#)] [[PubMed](#)]
12. Ruhling, S.; Kramer, F.; Schmutz, S.; Amor, S.; Jiangshan, Z.; Schmitz, C.; Kipp, M.; Hochstrasser, T. Visualization of the Breakdown of the Axonal Transport Machinery: A Comparative Ultrastructural and Immunohistochemical Approach. *Mol. Neurobiol.* **2019**, *56*, 3984–3998. [[CrossRef](#)] [[PubMed](#)]
13. Derakhshan, M.; Caramanos, Z.; Giacomini, P.S.; Narayanan, S.; Maranzano, J.; Francis, S.J.; Arnold, D.L.; Collins, D.L. Evaluation of automated techniques for the quantification of grey matter atrophy in patients with multiple sclerosis. *Neuroimage* **2010**, *52*, 1261–1267. [[CrossRef](#)] [[PubMed](#)]
14. Fisher, E.; Lee, J.C.; Nakamura, K.; Rudick, R.A. Gray matter atrophy in multiple sclerosis: A longitudinal study. *Ann. Neurol.* **2008**, *64*, 255–265. [[CrossRef](#)] [[PubMed](#)]
15. MacKenzie-Graham, A.; Rinek, G.A.; Avedisian, A.; Gold, S.M.; Frew, A.J.; Aguilar, C.; Lin, D.R.; Umeda, E.; Voskuhl, R.R.; Alger, J.R. Cortical atrophy in experimental autoimmune encephalomyelitis: In vivo imaging. *Neuroimage* **2012**, *60*, 95–104. [[CrossRef](#)] [[PubMed](#)]
16. Wood, T.C.; Simmons, C.; Hurley, S.A.; Vernon, A.C.; Torres, J.; Dell'Acqua, F.; Williams, S.C.; Cash, D. Whole-brain ex-vivo quantitative MRI of the cuprizone mouse model. *PeerJ* **2016**, *4*. [[CrossRef](#)]
17. Bergsland, N.; Horakova, D.; Dwyer, M.G.; Dolezal, O.; Seidl, Z.K.; Vaneckova, M.; Krasensky, J.; Havrdova, E.; Zivadinov, R. Subcortical and cortical gray matter atrophy in a large sample of patients with clinically isolated syndrome and early relapsing-remitting multiple sclerosis. *AJNR Am. J. Neuroradiol.* **2012**, *33*, 1573–1578. [[CrossRef](#)] [[PubMed](#)]
18. De Stefano, N.; Matthews, P.M.; Filippi, M.; Agosta, F.; De Luca, M.; Bartolozzi, M.L.; Guidi, L.; Ghezzi, A.; Montanari, E.; Cifelli, A.; et al. Evidence of early cortical atrophy in MS: Relevance to white matter changes and disability. *Neurology* **2003**, *60*, 1157–1162. [[CrossRef](#)]
19. Batista, S.; Zivadinov, R.; Hoogs, M.; Bergsland, N.; Heininen-Brown, M.; Dwyer, M.G.; Weinstock-Guttman, B.; Benedict, R.H. Basal ganglia, thalamus and neocortical atrophy predicting slowed cognitive processing in multiple sclerosis. *J. Neurol.* **2012**, *259*, 139–146. [[CrossRef](#)]
20. Houtchens, M.K.; Benedict, R.H.; Killiany, R.; Sharma, J.; Jaisani, Z.; Singh, B.; Weinstock-Guttman, B.; Guttman, C.R.; Bakshi, R. Thalamic atrophy and cognition in multiple sclerosis. *Neurology* **2007**, *69*, 1213–1223. [[CrossRef](#)]

21. Barkhof, F.; Calabresi, P.A.; Miller, D.H.; Reingold, S.C. Imaging outcomes for neuroprotection and repair in multiple sclerosis trials. *Nat. Rev. Neurol.* **2009**, *5*, 256–266. [[CrossRef](#)] [[PubMed](#)]
22. Sormani, M.P.; Arnold, D.L.; De Stefano, N. Treatment effect on brain atrophy correlates with treatment effect on disability in multiple sclerosis. *Ann. Neurol.* **2014**, *75*, 43–49. [[CrossRef](#)] [[PubMed](#)]
23. Wagenknecht, N.; Becker, B.; Scheld, M.; Beyer, C.; Clarner, T.; Hochstrasser, T.; Kipp, M. Thalamus Degeneration and Inflammation in Two Distinct Multiple Sclerosis Animal Models. *J. Mol. Neurosci.* **2016**, *60*, 102–114. [[CrossRef](#)] [[PubMed](#)]
24. Clarner, T.; Diederichs, F.; Berger, K.; Denecke, B.; Gan, L.; van der Valk, P.; Beyer, C.; Amor, S.; Kipp, M. Myelin debris regulates inflammatory responses in an experimental demyelination animal model and multiple sclerosis lesions. *Glia* **2012**, *60*, 1468–1480. [[CrossRef](#)] [[PubMed](#)]
25. Lindner, M.; Fokuhl, J.; Linsmeier, F.; Trebst, C.; Stangel, M. Chronic toxic demyelination in the central nervous system leads to axonal damage despite remyelination. *Neurosci. Lett.* **2009**, *453*, 120–125. [[CrossRef](#)]
26. Guglielmetti, C.; Veraart, J.; Roelant, E.; Mai, Z.; Daans, J.; Van Audekerke, J.; Naeyaert, M.; Vanhoutte, G.; Delgado, Y.P.R.; Praet, J.; et al. Diffusion kurtosis imaging probes cortical alterations and white matter pathology following cuprizone induced demyelination and spontaneous remyelination. *Neuroimage* **2016**, *125*, 363–377. [[CrossRef](#)]
27. Thiessen, J.D.; Zhang, Y.; Zhang, H.; Wang, L.; Buist, R.; Del Bigio, M.R.; Kong, J.; Li, X.M.; Martin, M. Quantitative MRI and ultrastructural examination of the cuprizone mouse model of demyelination. *NMR Biomed.* **2013**, *26*, 1562–1581. [[CrossRef](#)]
28. Wu, Q.Z.; Yang, Q.; Cate, H.S.; Kemper, D.; Binder, M.; Wang, H.X.; Fang, K.; Quick, M.J.; Marriott, M.; Kilpatrick, T.J.; et al. MRI identification of the rostral-caudal pattern of pathology within the corpus callosum in the cuprizone mouse model. *J. Magn Reson. Med.* **2008**, *27*, 446–453. [[CrossRef](#)]
29. Lapato, A.S.; Szu, J.I.; Hasselmann, J.P.C.; Khalaj, A.J.; Binder, D.K.; Tiwari-Woodruff, S.K. Chronic demyelination-induced seizures. *Neuroscience* **2017**, *346*, 409–422. [[CrossRef](#)]
30. Hoffmann, K.; Lindner, M.; Groticke, I.; Stangel, M.; Loscher, W. Epileptic seizures and hippocampal damage after cuprizone-induced demyelination in C57BL/6 mice. *Exp. Neurol.* **2008**, *210*, 308–321. [[CrossRef](#)]
31. Kipp, M.; Kiessling, M.C.; Hochstrasser, T.; Roggenkamp, C.; Schmitz, C. Design-Based Stereology for Evaluation of Histological Parameters. *J. Mol. Neurosci.* **2017**, *61*, 325–342. [[CrossRef](#)] [[PubMed](#)]
32. Fischbach, F.; Nedelcu, J.; Leopold, P.; Zhan, J.; Clarner, T.; Nellesen, L.; Beissel, C.; van Heuvel, Y.; Goswami, A.; Weis, J.; et al. Cuprizone-induced graded oligodendrocyte vulnerability is regulated by the transcription factor DNA damage-inducible transcript 3. *Glia* **2019**, *67*, 263–276. [[CrossRef](#)] [[PubMed](#)]
33. Sidman, R.L.; Angevine, J.B.; Pierce, E.T. *Atlas of the Mouse Brain and Spinal Cord*; Harvard University Press: Cambridge, UK, 1971; p. 261.
34. Hochstrasser, T.; Exner, G.L.; Nyamoya, S.; Schmitz, C.; Kipp, M. Cuprizone-Containing Pellets Are Less Potent to Induce Consistent Demyelination in the Corpus Callosum of C57BL/6 Mice. *J. Mol. Neurosci.* **2017**, *61*, 617–624. [[CrossRef](#)] [[PubMed](#)]
35. Chrzanowski, U.; Schmitz, C.; Horn-Bochtler, A.; Nack, A.; Kipp, M. Evaluation strategy to determine reliable demyelination in the cuprizone model. *Metab. Brain Dis.* **2019**, *34*, 681–685. [[CrossRef](#)] [[PubMed](#)]
36. Goldberg, J.; Clarner, T.; Beyer, C.; Kipp, M. Anatomical Distribution of Cuprizone-Induced Lesions in C57BL6 Mice. *J. Mol. Neurosci.* **2015**, *57*, 166–175. [[CrossRef](#)]
37. Skripuletz, T.; Lindner, M.; Kotsiari, A.; Garde, N.; Fokuhl, J.; Linsmeier, F.; Trebst, C.; Stangel, M. Cortical demyelination is prominent in the murine cuprizone model and is strain-dependent. *Am. J. Pathol.* **2008**, *172*, 1053–1061. [[CrossRef](#)] [[PubMed](#)]
38. Pott, F.; Gingele, S.; Clarner, T.; Dang, J.; Baumgartner, W.; Beyer, C.; Kipp, M. Cuprizone effect on myelination, astrogliosis and microglia attraction in the mouse basal ganglia. *Brain Res.* **2009**, *1305*, 137–149. [[CrossRef](#)]
39. Schmitz, C.; Bultmann, E.; Gube, M.; Korr, H. Neuron loss in the mouse hippocampus following prenatal injection of tritiated thymidine or saline. *Int. J. Dev. Neurosci.* **1999**, *17*, 185–190. [[CrossRef](#)]
40. Schmitz, C.; Hof, P. Design-based stereology in neuroscience. *Neurosci.* **2005**, *130*, 813–831. [[CrossRef](#)]
41. Schmitz, C.; Hof, P.R. Recommendations for straightforward and rigorous methods of counting neurons based on a computer simulation approach. *J. Chem. Neuroanat.* **2000**, *20*, 93–114. [[CrossRef](#)]
42. Brendel, M.; Probst, F.; Jaworska, A.; Overhoff, F.; Korzhova, V.; Albert, N.L.; Beck, R.; Lindner, S.; Gildehaus, F.J.; Baumann, K.; et al. Glial Activation and Glucose Metabolism in a Transgenic Amyloid Mouse Model.: A Triple-Tracer PET Study. *J. Nucl. Med.* **2016**, *57*, 954–960. [[CrossRef](#)] [[PubMed](#)]

43. Leopold, P.; Schmitz, C.; Kipp, M. Animal Weight Is an Important Variable for Reliable Cuprizone-Induced Demyelination. *J. Mol. Neurosci.* **2019**, *68*, 522–528. [[CrossRef](#)] [[PubMed](#)]
44. Esser, S.; Gopfrich, L.; Bihler, K.; Kress, E.; Nyamoya, S.; Tauber, S.C.; Clarner, T.; Stope, M.B.; Pufe, T.; Kipp, M.; et al. Toll-Like Receptor 2-Mediated Glial Cell Activation in a Mouse Model of Cuprizone-Induced Demyelination. *Mol. Neurobiol.* **2018**, *55*, 6237–6249. [[CrossRef](#)] [[PubMed](#)]
45. Cerina, M.; Narayanan, V.; Gobel, K.; Bittner, S.; Ruck, T.; Meuth, P.; Herrmann, A.M.; Stangel, M.; Gudi, V.; Skripuletz, T.; et al. The quality of cortical network function recovery depends on localization and degree of axonal demyelination. *Brain Behav. Immun.* **2017**, *59*, 103–117. [[CrossRef](#)] [[PubMed](#)]
46. Peterson, J.W.; Bo, L.; Mork, S.; Chang, A.; Trapp, B.D. Transected neurites, apoptotic neurons, and reduced inflammation in cortical multiple sclerosis lesions. *Ann. Neurol.* **2001**, *50*, 389–400. [[CrossRef](#)] [[PubMed](#)]
47. Klaver, R.; Popescu, V.; Voorn, P.; Galis-de Graaf, Y.; van der Valk, P.; de Vries, H.E.; Schenk, G.J.; Geurts, J.J. Neuronal and axonal loss in normal-appearing gray matter and subpial lesions in multiple sclerosis. *J. Neuropathol. Exp. Neurol.* **2015**, *74*, 453–458. [[CrossRef](#)]
48. Carassiti, D.; Altmann, D.R.; Petrova, N.; Pakkenberg, B.; Scaravilli, F.; Schmierer, K. Neuronal loss, demyelination and volume change in the multiple sclerosis neocortex. *Neuropathol. Appl. Neurobiol.* **2018**, *44*, 377–390. [[CrossRef](#)]
49. Chrzanowski, U.; Bhattarai, S.; Scheld, M.; Clarner, T.; Fallier-Becker, P.; Beyer, C.; Rohr, S.O.; Schmitz, C.; Hochstrasser, T.; Schweiger, F.; et al. Oligodendrocyte degeneration and concomitant microglia activation directs peripheral immune cells into the forebrain. *Neurochem. Int.* **2019**, *126*, 139–153. [[CrossRef](#)]
50. Ruther, B.J.; Scheld, M.; Drey Mueller, D.; Clarner, T.; Kress, E.; Brandenburg, L.O.; Swartenbroeckx, T.; Hoornaert, C.; Ponsaerts, P.; Fallier-Becker, P.; et al. Combination of cuprizone and experimental autoimmune encephalomyelitis to study inflammatory brain lesion formation and progression. *Glia* **2017**, *65*, 1900–1913. [[CrossRef](#)]
51. Scheld, M.; Ruther, B.J.; Grosse-Veldmann, R.; Ohl, K.; Tenbrock, K.; Drey Mueller, D.; Fallier-Becker, P.; Zendedel, A.; Beyer, C.; Clarner, T.; et al. Neurodegeneration Triggers Peripheral Immune Cell Recruitment into the Forebrain. *J. Neurosci.* **2016**, *36*, 1410–1415. [[CrossRef](#)]
52. Witte, M.E.; Bo, L.; Rodenburg, R.J.; Belien, J.A.; Musters, R.; Hazes, T.; Wintjes, L.T.; Smeitink, J.A.; Geurts, J.J.; De Vries, H.E.; et al. Enhanced number and activity of mitochondria in multiple sclerosis lesions. *J. Pathol.* **2009**, *219*, 193–204. [[CrossRef](#)] [[PubMed](#)]
53. Ohno, N.; Chiang, H.; Mahad, D.J.; Kidd, G.J.; Liu, L.; Ransohoff, R.M.; Sheng, Z.H.; Komuro, H.; Trapp, B.D. Mitochondrial immobilization mediated by syntrophin facilitates survival of demyelinated axons. *Proc. Natl. Acad. Sci. USA* **2014**, *111*, 9953–9958. [[CrossRef](#)] [[PubMed](#)]
54. Rodriguez, M.; Scheithauer, B. Ultrastructure of Multiple Sclerosis. *Ultrastruct. Pathol.* **1994**, *18*, 3–13. [[CrossRef](#)] [[PubMed](#)]
55. Ludwin, S.K.; Johnson, E.S. Evidence for a “dying-back” gliopathy in demyelinating disease. *Ann. Neurol.* **1981**, *9*, 301–305. [[PubMed](#)]
56. Prineas, J.W.; Parratt, J.D. Oligodendrocytes and the early multiple sclerosis lesion. *Ann. Neurol.* **2012**, *72*, 18–31. [[CrossRef](#)]
57. Buschmann, J.P.; Berger, K.; Awad, H.; Clarner, T.; Beyer, C.; Kipp, M. Inflammatory response and chemokine expression in the white matter corpus callosum and gray matter cortex region during cuprizone-induced demyelination. *J. Mol. Neurosci.* **2012**, *48*, 66–76. [[CrossRef](#)] [[PubMed](#)]
58. Kipp, M.; Wagenknecht, N.; Beyer, C.; Samer, S.; Wuerfel, J.; Nikoubashman, O. Thalamus pathology in multiple sclerosis: From biology to clinical application. *Cell. Mol. Life Sci.* **2015**, *72*, 1127–1147. [[CrossRef](#)] [[PubMed](#)]
59. Wylezinska, M.; Cifelli, A.; Jezard, P.; Palace, J.; Alecci, M.; Matthews, P.M. Thalamic neurodegeneration in relapsing-remitting multiple sclerosis. *Neurology* **2003**, *60*, 1949–1954. [[CrossRef](#)]
60. Cifelli, A.; Arridge, M.; Jezard, P.; Esiri, M.M.; Palace, J.; Matthews, P.M. Thalamic neurodegeneration in multiple sclerosis. *Ann. Neurol.* **2002**, *52*, 650–653. [[CrossRef](#)]
61. Schoonheim, M.M.; Popescu, V.; Rueda Lopes, F.C.; Wiebenga, O.T.; Vrenken, H.; Douw, L.; Polman, C.H.; Geurts, J.J.; Barkhof, F. Subcortical atrophy and cognition: Sex effects in multiple sclerosis. *Neurology* **2012**, *79*, 1754–1761. [[CrossRef](#)]

62. Magon, S.; Chakravarty, M.M.; Amann, M.; Weier, K.; Naegelin, Y.; Andelova, M.; Radue, E.W.; Stippich, C.; Lerch, J.P.; Kappos, L.; et al. Label-fusion-segmentation and deformation-based shape analysis of deep gray matter in multiple sclerosis: The impact of thalamic subnuclei on disability. *Hum. Brain Mapp.* **2014**, *35*, 4193–4203. [[CrossRef](#)] [[PubMed](#)]
63. Herholz, K. Perfusion SPECT and FDG-PET. *Int. Psychogeriatr.* **2011**, *23*, S25–S31. [[CrossRef](#)] [[PubMed](#)]
64. Kleinberger, G.; Brendel, M.; Mracsko, E.; Wefers, B.; Groeneweg, L.; Xiang, X.; Focke, C.; Deussing, M.; Suarez-Calvet, M.; Mazaheri, F.; et al. The FTD-like syndrome causing TREM2 T66M mutation impairs microglia function, brain perfusion, and glucose metabolism. *EMBO J.* **2017**, *36*, 1837–1853. [[CrossRef](#)] [[PubMed](#)]
65. Irvine, K.A.; Blakemore, W.F. Age increases axon loss associated with primary demyelination in cuprizone-induced demyelination in C57BL/6 mice. *J. Neuroimmunol.* **2006**, *175*, 69–76. [[CrossRef](#)] [[PubMed](#)]
66. Nikic, I.; Merkler, D.; Sorbara, C.; Brinkoetter, M.; Kreutzfeldt, M.; Bareyre, F.M.; Bruck, W.; Bishop, D.; Misgeld, T.; Kerschensteiner, M. A reversible form of axon damage in experimental autoimmune encephalomyelitis and multiple sclerosis. *Nat. Med.* **2011**, *17*, 495–499. [[CrossRef](#)] [[PubMed](#)]
67. Carlton, W.W. Spongiform encephalopathy induced in rats and guinea pigs by cuprizone. *Exp. Mol. Pathol.* **1969**, *10*, 274–287. [[CrossRef](#)]
68. De Stefano, N.; Airas, L.; Grigoriadis, N.; Mattle, H.P.; O’Riordan, J.; Oreja-Guevara, C.; Sellebjerg, F.; Stankoff, B.; Walczak, A.; Wiendl, H.; et al. Clinical relevance of brain volume measures in multiple sclerosis. *CNS Drugs* **2014**, *28*, 147–156. [[CrossRef](#)] [[PubMed](#)]
69. Jurgens, T.; Jafari, M.; Kreutzfeldt, M.; Bahn, E.; Bruck, W.; Kerschensteiner, M.; Merkler, D. Reconstruction of single cortical projection neurons reveals primary spine loss in multiple sclerosis. *Brain* **2016**, *139*, 39–46. [[CrossRef](#)] [[PubMed](#)]
70. Lee, M.A.; Blamire, A.M.; Pendlebury, S.; Ho, K.H.; Mills, K.R.; Styles, P.; Palace, J.; Matthews, P.M. Axonal injury or loss in the internal capsule and motor impairment in multiple sclerosis. *Arch. Neurol.* **2000**, *57*, 65–70. [[CrossRef](#)] [[PubMed](#)]



© 2019 by the authors. Licensee MDPI, Basel, Switzerland. This article is an open access article distributed under the terms and conditions of the Creative Commons Attribution (CC BY) license (<http://creativecommons.org/licenses/by/4.0/>).

7. References

1. The Multiple Sclerosis International Federation (MSIF) S 2020. Atlas of MS 3 rd edition. *Mult Scler Int Fed (MSIF)*, Sept 2020. 2020;(September):1–37.
2. Orton SM, Herrera BM, Yee IM, Valdar W, Ramagopalan S V., Sadovnick AD, et al. Sex ratio of multiple sclerosis in Canada: a longitudinal study. *Lancet Neurol*. 2006;5(11):932–6.
3. Fred D. Lublin. Defining the clinical course of multiple sclerosis: Results of an international survey. *Neurology* [Internet]. 1996 Mar 3;84(9):963. Available from: <http://www.neurology.org/cgi/doi/10.1212/01.wnl.0000462309.76486.c5>
4. Noseworthy JH, Lucchinetti C, Rodriguez M, Weinshenker BG. Multiple sclerosis. *N Engl J Med*. 2000;(343):938–952.
5. Miller DH, Leary SM. Primary-progressive multiple sclerosis. *Lancet Neurol*. 2007;6:903–12.
6. Olsson T, Barcellos LF, Alfredsson L. Interactions between genetic, lifestyle and environmental risk factors for multiple sclerosis. *Nat Rev Neurol* [Internet]. 2016;13(1):26–36. Available from: <http://dx.doi.org/10.1038/nrneurol.2016.187>
7. Alter M, Kahana E, Loewenson R. Migration and risk of multiple sclerosis. *Neurology*. 1978;28(11):1089–93.
8. Dean G, Kurtzke JF. On the Risk of Multiple Sclerosis According to Age at Immigration to South Africa. *Br Med J*. 1971;3(5777):725–9.
9. Detels R, Visscher BR, Haile RW, Malmgren RM, Dudley JP, Coulson AH. Multiple sclerosis and age at migration. *Am J Epidemiol*. 1978;108(5):386–93.
10. Patsopoulos NA, Barcellos LF, Hintzen RQ, Schaefer C, van Duijn CM, Noble JA, et al. Fine-Mapping the Genetic Association of the Major Histocompatibility Complex in Multiple Sclerosis: HLA and Non-HLA Effects. *PLoS Genet*. 2013;9(11).
11. Sospedra M, Martin R. Immunology of multiple sclerosis. *Annu Rev Immunol*. 2005;23:683–747.
12. Hohlfeld R, Dornmair K, Meinl E, Wekerle H. The search for the target antigens of multiple sclerosis, part 1: Autoreactive CD4+ T lymphocytes as pathogenic effectors and therapeutic targets. *Lancet Neurol* [Internet]. 2016;15(2):198–209. Available from: [http://dx.doi.org/10.1016/S1474-4422\(15\)00334-8](http://dx.doi.org/10.1016/S1474-4422(15)00334-8)
13. Stys PK, Zamponi GW, Van Minnen J, Geurts JGG. Erratum: Will the real multiple sclerosis please stand up? (*Nature Reviews Neuroscience* (2012) 13 (507–514)). *Nat Rev Neurosci* [Internet]. 2012;13(8):597. Available from: <http://dx.doi.org/10.1038/nrn3275>
14. Trapp BD, Nave KA. Multiple sclerosis: An immune or neurodegenerative disorder? *Annu Rev Neurosci*. 2008;31:247–69.
15. Barnett MH, Prineas JW. Relapsing and Remitting Multiple Sclerosis: Pathology of the Newly Forming Lesion. *Ann Neurol*. 2004;55(4):458–68.
16. Lucchinetti C, Brück W, Parisi J, Scheithauer B, Rodriguez M, Lassmann H. A quantitative analysis of oligodendrocytes in multiple sclerosis lesions. A study of 113 cases. *Brain*. 1999;122(12):2279–95.
17. Prodinger C, Bunse J, Krüger M, Schiefenhövel F, Brandt C, Laman JD, et al. CD11c-expressing cells reside in the juxtavascular parenchyma and extend processes into the glia limitans of the mouse nervous system. *Acta Neuropathol*. 2011;121(4):445–58.
18. Mohammad MG, Tsai VWW, Ruitenber MJ, Hassanpour M, Li H, Hart PH, et al. Immune cell trafficking from the brain maintains CNS immune tolerance. *J Clin Invest*. 2014;124(3):1228–41.
19. Xie L, Kang H, Xu Q, Chen MJ, Liao Y, Thiyagarajan M, et al. Sleep drives metabolite clearance from the adult brain. *Science* (80-). 2013;342(6156):373–7.
20. Baxi EG, DeBruin J, Tosi DM, Grishkan I V., Smith MD, Kirby LA, et al. Transfer

- of myelin-reactive Th17 cells impairs endogenous remyelination in the central nervous system of cuprizone-fed mice. *J Neurosci*. 2015;35(22):8626–39.
21. Scheld M, Rütther BJ, Große-Veldmann R, Ohl K, Tenbrock K, Dreytmüller D, et al. Neurodegeneration triggers peripheral immune cell recruitment into the forebrain. *J Neurosci*. 2016;36(4):1410–5.
 22. Kornek B, Storch MK, Weissert R, Wallstroem E, Stefferl A, Olsson T, et al. Multiple sclerosis and chronic autoimmune encephalomyelitis: A comparative quantitative study of axonal injury in active, inactive, and remyelinated lesions. *Am J Pathol* [Internet]. 2000;157(1):267–76. Available from: [http://dx.doi.org/10.1016/S0002-9440\(10\)64537-3](http://dx.doi.org/10.1016/S0002-9440(10)64537-3)
 23. Ferguson B, Matyszak MK, Esiri MM, Perry VH. Axonal damage in acute multiple sclerosis lesions. *Brain*. 1997;120(3):393–9.
 24. Burton E V., Greenberg BM, Frohman EM. Optic neuritis: A mechanistic view. *Pathophysiology* [Internet]. 2011;18(1):81–92. Available from: <http://dx.doi.org/10.1016/j.pathophys.2010.04.009>
 25. Irvine KA, Blakemore WF. Remyelination protects axons from demyelination-associated axon degeneration. *Brain*. 2008;131(6):1464–77.
 26. Waxman SG. Axonal conduction and injury in multiple sclerosis: The role of sodium channels. *Nat Rev Neurosci*. 2006;7(12):932–41.
 27. Franklin RJM, Ffrench-Constant C. Remyelination in the CNS: From biology to therapy. *Nat Rev Neurosci*. 2008;9(11):839–55.
 28. Nikić I, Merkler D, Sorbara C, Brinkoetter M, Kreutzfeldt M, Bareyre FM, et al. A reversible form of axon damage in experimental autoimmune encephalomyelitis and multiple sclerosis. *Nat Med*. 2011;17(4):495–9.
 29. Tomassini V, Matthews PM, Thompson AJ, Fuglo D, Geurts JJ, Johansen-Berg H, et al. Neuroplasticity and functional recovery in multiple sclerosis. *Nat Rev Neurol* [Internet]. 2012;8(11):635–46. Available from: <http://dx.doi.org/10.1038/nrneurol.2012.179>
 30. Enzinger C, Barkhof F, Ciccarelli O, Filippi M, Kappos L, Rocca MA, et al. Nonconventional MRI and microstructural cerebral changes in multiple sclerosis. *Nat Rev Neurol* [Internet]. 2015;11(12):676–86. Available from: <http://dx.doi.org/10.1038/nrneurol.2015.194>
 31. Tremlett H, Zhao Y, Joseph J, Devonshire V, Adams D, Craig D, et al. Relapses in multiple sclerosis are age- and time-dependent. *J Neurol Neurosurg Psychiatry*. 2008;79(12):1368–74.
 32. Anderson VM, Fox NC, Miller DH. Magnetic resonance imaging measures of brain atrophy in multiple sclerosis. *J Magn Reson Imaging*. 2006;23(5):605–18.
 33. Filippi M, Rocca MA. MRI evidence for multiple sclerosis as a diffuse disease of the central nervous system. *J Neurol*. 2005;252(SUPPL. 5):16–24.
 34. Cree BAC, Gourraud PA, Oksenberg JR, Bevan C, Crabtree-Hartman E, Gelfand JM, et al. Long-term evolution of multiple sclerosis disability in the treatment era. *Ann Neurol*. 2016;80(4):499–510.
 35. Mahad DH, Trapp BD, Lassmann H. Pathological mechanisms in progressive multiple sclerosis. *Lancet Neurol* [Internet]. 2015;14(2):183–93. Available from: [http://dx.doi.org/10.1016/S1474-4422\(14\)70256-X](http://dx.doi.org/10.1016/S1474-4422(14)70256-X)
 36. Feinstein A, Freeman J, Lo AC. Treatment of progressive multiple sclerosis: What works, what does not, and what is needed. *Lancet Neurol* [Internet]. 2015;14(2):194–207. Available from: [http://dx.doi.org/10.1016/S1474-4422\(14\)70231-5](http://dx.doi.org/10.1016/S1474-4422(14)70231-5)
 37. La Mantia L, Vacchi L, Rovaris M, Di Pietrantonj C, Ebers G, Fredrikson S, et al. Interferon β for secondary progressive multiple sclerosis: A systematic review. *J Neurol Neurosurg Psychiatry*. 2013;84(4):420–6.
 38. Meinl E, Krumbholz M, Derfuss T, Junker A, Hohlfeld R. Compartmentalization of inflammation in the CNS: A major mechanism driving progressive multiple sclerosis. *J Neurol Sci*. 2008;274(1–2):42–4.
 39. Behrangi N, Fischbach F, Kipp M. Mechanism of Siponimod: Anti-Inflammatory

- and Neuroprotective Mode of Action. *Cells*. 2019;8(1):24.
40. Kappos L, Bar-Or A, Cree BAC, Fox RJ, Giovannoni G, Gold R, et al. Siponimod versus placebo in secondary progressive multiple sclerosis (EXPAND): a double-blind, randomised, phase 3 study. *Lancet*. 2018;391(10127):1263–73.
 41. Kutzelnigg A, Lucchinetti CF, Stadelmann C, Brück W, Rauschka H, Bergmann M, et al. Cortical demyelination and diffuse white matter injury in multiple sclerosis. *Brain*. 2005;128(11):2705–12.
 42. Seewann A, Vrenken H, van der Valk P, Blezer ELA, Knol DL, Castelijns JA, et al. Diffusely Abnormal White Matter in Chronic Multiple Sclerosis. *Arch Neurol*. 2009;66(5):601–9.
 43. Trapp BD, Peterson J, Ransohoff RM, Rudick R, Mörk S, Bö L. Axonal Transection in the Lesions of Multiple Sclerosis. *N Engl J Med*. 1998;338(5):278–85.
 44. Evangelou N, Esiri MM, Smith S, Palace J MP. Quantitative pathological evidence for axonal loss in normal appearing white matter in multiple sclerosis. *Off J Am Neurol Assoc Child Neurol Soc*. 2000;47(3):361–5.
 45. Lassmann H, Van Horssen J, Mahad D. Progressive multiple sclerosis: Pathology and pathogenesis. *Nat Rev Neurol* [Internet]. 2012;8(11):647–56. Available from: <http://dx.doi.org/10.1038/nrneurol.2012.168>
 46. Prineas JW, Kwon EE, Cho ES, Sharer LR, Barnett MH, Oleszak EL, et al. Immunopathology of secondary-progressive multiple sclerosis. *Ann Neurol*. 2001;50(5):646–57.
 47. Tallantyre EC, Bø L, Al-Rawashdeh O, Owens T, Polman CH, Lowe JS, et al. Clinico-pathological evidence that axonal loss underlies disability in progressive multiple sclerosis. *Mult Scler*. 2010;16(4):406–11.
 48. Hochstrasser T, Jiangshan Z, Rühling S, Schmitz C, Kipp M. Do pre-clinical multiple sclerosis models allow us to measure neurodegeneration and clinical progression? *Expert Rev Neurother* [Internet]. 2018;18(5):351–3. Available from: <https://doi.org/10.1080/14737175.2018.1459190>
 49. Kipp M, Nyamoya S, Hochstrasser T, Amor S. Multiple sclerosis animal models: a clinical and histopathological perspective. *Brain Pathol*. 2017;27(2):123–37.
 50. Robinson AP, Harp CT, Noronha A, Miller SD. The experimental autoimmune encephalomyelitis (EAE) model of MS. utility for understanding disease pathophysiology and treatment. [Internet]. 1st ed. Vol. 122, *Handbook of Clinical Neurology*. Elsevier B.V.; 2014. 173–189 p. Available from: <http://dx.doi.org/10.1016/B978-0-444-52001-2.00008-X>
 51. Nilsson G, Erdtman H, Lindstedt G, Kinell P-O. A New Colour Reaction on Copper and Certain Carbonyl Compounds. Vol. 4, *Acta Chemica Scandinavica*. 1950. p. 205–205.
 52. Carlton WW. Response of mice to the chelating agents sodium diethyldithiocarbamate, α -benzoinoxime, and biscyclohexanone oxaldihydrazone. *Toxicol Appl Pharmacol*. 1966;8(3):512–21.
 53. Carlton WW. Studies on the induction of hydrocephalus and spongy degeneration by cuprizone feeding and attempts to antidote the toxicity. *Life Sci*. 1967;6(1):11–9.
 54. Draheim T, Liessem A, Scheld M, Wilms F, Weißflog M, Denecke B, et al. Activation of the astrocytic Nrf2/ARE system ameliorates the formation of demyelinating lesions in a multiple sclerosis animal model. *Glia*. 2016;64(12):2219–30.
 55. Kipp M, Clarner T, Dang J, Copray S, Beyer C. The cuprizone animal model: New insights into an old story. *Acta Neuropathol*. 2009;118(6):723–36.
 56. Praet J, Guglielmetti C, Berneman Z, Van der Linden A, Ponsaerts P. Cellular and molecular neuropathology of the cuprizone mouse model: Clinical relevance for multiple sclerosis. *Neurosci Biobehav Rev* [Internet]. 2014;47:485–505. Available from: <http://dx.doi.org/10.1016/j.neubiorev.2014.10.004>
 57. Bakker DA, Ludwin SK. Blood-brain barrier permeability during Cuprizone-

- induced demyelination. Implications for the pathogenesis of immune-mediated demyelinating diseases. *J Neurol Sci.* 1987;78(2):125–37.
58. Blakemore WF. Observations on oligodendrocyte degeneration, the resolution of status spongiosus and remyelination in cuprizone intoxication in mice. *J Neurocytol.* 1972;1(4):413–26.
 59. Clarner T, Janssen K, Nellessen L, Stangel M, Skripuletz T, Krauspe B, et al. CXCL10 Triggers Early Microglial Activation in the Cuprizone Model. *J Immunol.* 2015;194(7):3400–13.
 60. Groebe A, Clarner T, Baumgartner W, Dang J, Beyer C, Kipp M. Cuprizone treatment induces distinct demyelination, astrogliosis, and microglia cell invasion or proliferation in the mouse cerebellum. *Cerebellum.* 2009;8(3):163–74.
 61. Skripuletz T, Lindner M, Kotsiari A, Garde N, Fokuhl J, Linsmeier F, et al. Cortical demyelination is prominent in the murine cuprizone model and is strain-dependent. *Am J Pathol [Internet].* 2008;172(4):1053–61. Available from: <http://dx.doi.org/10.2353/ajpath.2008.070850>
 62. Höflich KM, Beyer C, Clarner T, Schmitz C, Nyamoya S, Kipp M, et al. Acute axonal damage in three different murine models of multiple sclerosis: A comparative approach. *Brain Res.* 2016;1650:125–33.
 63. Goldberg J, Clarner T, Beyer C, Kipp M. Anatomical Distribution of Cuprizone-Induced Lesions in C57BL6 Mice. *J Mol Neurosci.* 2015;57(2):166–75.
 64. Ransohoff RM. Animal models of multiple sclerosis: The good, the bad and the bottom line. *Nat Neurosci [Internet].* 2012;15(8):1074–7. Available from: <http://dx.doi.org/10.1038/nn.3168>
 65. Vega-Riquer JM, Mendez-Victoriano G, Morales-Luckie RA, Gonzalez-Perez O. Five Decades of Cuprizone, an Updated Model to Replicate Demyelinating Diseases. *Curr Neuropharmacol.* 2019;17(2):129–41.
 66. Torkildsen, Brunborg LA, Myhr KM, Bø L. The cuprizone model for demyelination. *Acta Neurol Scand.* 2008;117(SUPPL. 188):72–6.
 67. Zhan J, Mann T, Joost S, Behrangi N, Frank M, Kipp M. The Cuprizone Model: Dos and Do Nots. *Cells.* 2020;9(4):843.
 68. Sorbara CD, Wagner NE, Ladwig A, Nikić I, Merkler D, Kleele T, et al. Pervasive axonal transport deficits in multiple sclerosis models. *Neuron.* 2014;84(6):1183–90.
 69. Kuhlmann T, Lingfeld G, Bitsch A, Schuchardt J, Brück W. Acute axonal damage in multiple sclerosis is most extensive in early disease stages and decreases over time. *Brain.* 2002;125(10):2202–12.
 70. Groemer TW, Thiel CS, Holt M, Riedel D, Hua Y, Hüve J, et al. Amyloid precursor protein is trafficked and secreted via synaptic vesicles. *PLoS One.* 2011;6(4).
 71. Tyan SH, Shih AYJ, Walsh JJ, Maruyama H, Sarsoza F, Ku L, et al. Amyloid precursor protein (APP) regulates synaptic structure and function. *Mol Cell Neurosci [Internet].* 2012;51(1–2):43–52. Available from: <http://dx.doi.org/10.1016/j.mcn.2012.07.009>
 72. Calabrese M, Romualdi C, Poretto V, Favaretto A, Morra A, Rinaldi F, et al. The changing clinical course of multiple sclerosis: A matter of gray matter. *Ann Neurol.* 2013;74(1):76–83.
 73. Pirko I, Lucchinetti CF, Sriram S, Bakshi R. Gray matter involvement in multiple sclerosis. *Neurology.* 2007;68(9):634–42.
 74. Kutzelnigg A, Lassmann H. Cortical lesions and brain atrophy in MS. *J Neurol Sci.* 2005;233(1–2):55–9.
 75. Bermel RA, Bakshi R. The measurement and clinical relevance of brain atrophy in multiple sclerosis. *Lancet Neurol.* 2006;5(2):158–70.
 76. Dalton CM, Brex PA, Jenkins R, Fox NC, Miszkiel KA, Crum WR, et al. Progressive ventricular enlargement in patients with clinically isolated syndromes is associated with the early development of multiple sclerosis. *J*

-
- Neurol Neurosurg Psychiatry. 2002;73(2):141–7.
77. Rudick RA, Lee JC, Nakamura K, Fisher E. Gray matter atrophy correlates with MS disability progression measured with MSFC but not EDSS. *J Neurol Sci* [Internet]. 2009;282(1–2):106–11. Available from: <http://dx.doi.org/10.1016/j.jns.2008.11.018>
 78. van Munster CEP, Uitdehaag BMJ. Outcome Measures in Clinical Trials for Multiple Sclerosis. *CNS Drugs*. 2017;31(3):217–36.
 79. Barkhof F, Calabresi PA, Miller DH, Reingold SC. reviews Imaging outcomes for neuroprotection and repair in multiple sclerosis trials. 2009;M(May):256–66.
 80. Sormani MP, Arnold DL, Stefano N De. Treatment Effect on Brain Atrophy Correlates with Treatment Effect on Disability in Multiple Sclerosis. 2014;43–9.
 81. Kipp M, Kiessling MC, Hochstrasser T, Roggenkamp C, Schmitz C. Design-Based Stereology for Evaluation of Histological Parameters. *J Mol Neurosci* [Internet]. 2017;61(3):325–42. Available from: <http://dx.doi.org/10.1007/s12031-016-0858-9>
 82. Wagenknecht N, Becker B, Scheld M, Beyer C, Clarner T, Hochstrasser T, et al. Thalamus Degeneration and Inflammation in Two Distinct Multiple Sclerosis Animal Models. *J Mol Neurosci* [Internet]. 2016;60(1):102–14. Available from: <http://dx.doi.org/10.1007/s12031-016-0790-z>
 83. Batista S, Zivadinov R, Hoogs M, Bergsland N, Heininen-Brown M, Dwyer MG, et al. Basal ganglia, thalamus and neocortical atrophy predicting slowed cognitive processing in multiple sclerosis. *J Neurol*. 2012;259(1):139–46.
 84. Magon S, Chakravarty MM, Amann M, Weier K, Naegelin Y, Andelova M, et al. Label-fusion-segmentation and deformation-based shape analysis of deep gray matter in multiple sclerosis: The impact of thalamic subnuclei on disability. *Hum Brain Mapp*. 2014;35(8):4193–203.